The Astronomical Journal, 125:13–31, 2003 January

A SEARCH FOR Lyα EMITTERS AT REDSHIFT 3.7[1]

Shinobu S. Fujita,[2] Masaru Ajiki,[2] Yasuhiro Shioya,[2] Tohru Nagao,[2] Takashi Murayama,[2] Yoshiaki Taniguchi,[2] Sadanori Okamura,[3,4] Masami Ouchi,[3] Kazuhiro Shimasaku,[3,4] Mamoru Doi,[5] Hisanori Furusawa,[3] Masaru Hamabe,[6] Masahiko Kimura,[7] Yutaka Komiyama,[8] Masayuki Miyazaki,[3] Satoshi Miyazaki,[9] Fumiaki Nakata,[3] Maki Sekiguchi,[7] Masafumi Yagi,[3] Naoki Yasuda,[9] Yuichi Matsuda,[10] Hajime Tamura,[10] Tomoki Hayashino,[10] Keiichi Kodaira,[11] Hiroshi Karoji,[9] Toru Yamada,[9] Kouji Ohta,[12] and Masayuki Umemura[13]

Received 2002 March 18; accepted 2002 September 18

ABSTRACT

We present the results of a survey for emission-line objects, based on optical intermediate-band ($\lambda_c = 5736$ Å and $\Delta\lambda = 280$ Å) and broadband (B, V, R, and i') observations of the Subaru/XMM-Newton Deep Field with the 8.2 m Subaru telescope and the Subaru Prime Focus Camera (Suprime-Cam). All the data were obtained during the guaranteed time observations of the Suprime-Cam instrument. The intermediate-band image covered a sky area of $10\farcm62 \times 12\farcm40 \approx 132$ arcmin^2 in the Subaru/XMM-Newton Deep Field (Ouchi et al.). Using this image, we found 23 emission-line sources whose observed emission-line equivalent widths are greater than 250 Å. Their optical multicolor properties indicate that six emission-line sources are Lyα emitters at $z \approx 3.7$ ($\Delta z \approx 0.22$). They are either intense starburst galaxies or active galactic nuclei–like quasars at $z \approx 3.7$. Two more emission-line sources may also be Lyα emitters at $z \approx 3.7$, although their multicolor properties are marginal. Among the remaining 15 emission-line objects, eight objects appear to be strong emission-line galaxies at lower redshift; e.g., [O II] λ3727 emitters at $z \approx 0.54$, Hβ at $z \approx 0.18$, or [O III] λ5007 emitters at $z \approx 0.15$. The remaining seven objects are unclassified because they are too faint to be detected in broadband images. We discuss the observational properties of these strong emission-line sources. In particular, our data allow us to estimate the star formation density at $z \approx 3.7$ for the first time.

Key words: cosmology: observations — early universe — galaxies: evolution — galaxies: formation

1. INTRODUCTION

It has often been argued that forming galaxies at high redshifts experience very luminous starbursts and thus could be very bright in line emission, such as the Lyα and [O II] λ3727 emission lines (e.g., Partridge & Peebles 1967; Larson 1974; Meier 1976). However, although many attempts have been made to search for such very strong emission-line sources at high redshift (e.g., Pritchet 1994; see also Pahre & Djorgovski 1995; Thompson, Mannucci, & Beckwith 1996), by the mid 1990s most of these searches had failed, except for some successful surveys around known high-z objects, such as quasars and radio galaxies (Hu & McMahon 1996; Hu, McMahon, & Egami 1996; Petitjean et al. 1996; Pascarelle et al. 1996; Keel et al. 1999). Consequently, the Lyman-break method (or the broadband, color-selection method) has been mainly used to investigate observational properties of high-z galaxies for the past several years (Steidel et al. 1996a, 1996b, 1999; Cowie et al. 1996; Lanzetta, Yahil, & Fernandez-Soto 1996; Madau et al. 1996; Yahata et al. 2000; Ouchi et al. 2001).

Recently, however, new attempts with 10 m class telescopes have revealed the presence of Lyα emitters in blank fields at high redshift (Cowie & Hu 1998, hereafter CH98; see also Hu, McMahon, & Cowie 1999; Ouchi et al. 2003; Hu et al. 2002). Subsequently, Steidel et al. (2000, hereafter S00) also succeeded in finding a number of high-z Lyα emitters in the SSA22 blank field. Furthermore, Kudritzki et al. (2000, hereafter K00) have identified nine Lyα emitters at $z \approx 3.1$ during the course of their narrowband imaging survey aimed at looking for intracluster planetary nebulae in the Virgo Cluster (Mendez et al. 1997). These surveys have reinforced the potential importance of the search for high-z Lyα emitters. Thus deep imaging surveys with narrowband filters are now considered to be a powerful tool in this era of 10 m class telescopes to probe the Lyα emission from high-z young galaxies and active galactic nuclei–like quasars. Such surveys for high-z emission-line sources provide us with very important information not only on the formation and evolution of galaxies but also on the cosmic reionization process at very high redshift (e.g., Loeb & Barkana 2001 and references therein).

[1] Based on data collected at Subaru Telescope, which is operated by the National Astronomical Observatory of Japan.

[2] Astronomical Institute, Graduate School of Science, Tohoku University, Aramaki, Aoba, Sendai 980-8578, Japan.
[3] Department of Astronomy, Graduate School of Science, University of Tokyo, Tokyo 113-0033, Japan.
[4] Research Center for the Early Universe, School of Science, University of Tokyo, Tokyo 113-0033, Japan.
[5] Institute of Astronomy, Graduate School of Science, University of Tokyo, Mitaka, Tokyo 181-0015, Japan.
[6] Department of Mathematical and Physical Sciences, Faculty of Science, Japan Women's University, Tokyo 112-8681, Japan.
[7] Institute for Cosmic Ray Research, University of Tokyo, Kashiwa, Chiba 277-8582, Japan.
[8] Subaru Telescope, National Astronomical Observatory, 650 North A'ohoku Place, Hilo, HI 96720.
[9] National Astronomical Observatory, Mitaka, Tokyo 181-8588, Japan.
[10] Research Center for Neutrino Science, Graduate School of Science, Tohoku University, Aramaki, Aoba, Sendai 980-8578, Japan.
[11] The Graduate University for Advanced Studies, Shonan Village, Hayama, Kanagawa 240-0193, Japan.
[12] Department of Astronomy, Graduate School of Science, Kyoto University, Kitashirakawa, Sakyo, Kyoto 606-8502, Japan.
[13] Center for Computational Physics, University of Tsukuba, 1-1-1 Tennodai, Tsukuba 305-8571, Japan.

However, such surveys for emission-line galaxies with narrowband filters are limited in that survey volumes are so small because of narrower band widths (e.g., ~100 Å). In order to gain survey volumes, we need very wide field CCD cameras on 10 m class telescopes. Fortunately, the Subaru 8.2 m telescope (Kaifu 1998) at Mauna Kea Observatories has the wide-field (a $34' \times 27'$ field of view) prime-focus camera, Suprime-Cam (Miyazaki et al. 1998). This camera enables us to carry out narrowband imaging surveys for high-z emission-line objects.[14]

For this purpose we made a new filter system, which consists of 20 filters with the spectral resolution of $R = 23$, covering from 4000 to 9500 Å (Hayashino et al. 2000; Taniguchi 2001; Shioya et al. 2002). Its spectral resolution is not higher than that of typical narrowband filters used for Lyα-emitter searches; e.g., $R = 70$ with the central wavelength $\lambda_c = 5390$ Å and the bandwidth of $\Delta\lambda = 77$ Å (S00), and $R = 62$ with $\lambda_c = 4970$ Å and $\Delta\lambda = 80$ Å (S00). However, our intermediate-band filter system (called the IA system, which means the intermediate-band filter set A) is useful for detecting strong emission-line sources whose emission-line equivalent widths exceed 250 Å in the observed frame. Further, our system covers the entire optical wavelength range, and thus we will be able to carry out a full range of systematic searches for strong emission-line sources at various redshifts from $z \approx 2.2$ to $z \approx 6.9$ (Taniguchi 2001).

During the commissioning phase of Suprime-Cam on the Subaru telescope we made an imaging survey for Lyα emitters at $z \approx 3.7$ in the Subaru/XMM-Newton field (Ouchi et al. 2001), using one of the IA filters (IA574, $\lambda_c = 5736$ Å and $\Delta\lambda = 280$ Å). In this paper we present our first results of this intermediate-band imaging survey.

Throughout this paper magnitudes are given in the AB system. We adopt a flat universe with $\Omega_{\rm matter} = 0.3$, $\Omega_\Lambda = 0.7$, and $h = 0.7$, where $h = H_0/(100\ {\rm km\ s^{-1}\ Mpc^{-1}})$.

2. OBSERVATIONS AND DATA REDUCTION

2.1. *Observations*

As described in Ouchi et al. (2001; see also Ouchi 2001), we have obtained deep and wide-field B-, V-, R-, and i'-band imaging data of a central $30' \times 24'$ area in the Subaru/XMM-Newton Deep Survey Field centered at $\alpha({\rm J2000.0}) = 2^{\rm h}18^{\rm m}00^{\rm s}$ and $\delta({\rm J2000.0}) = -5^\circ 12' 00''$, using Suprime-Cam (Miyazaki et al. 1998) on the Subaru telescope during a period between 2000 August and 2000 November. In addition to these broadband image data, we obtained an intermediate-band image using the IA filter IA574 ($\lambda_c = 5736$ Å and $\Delta\lambda = 280$ Å) in 2000 August. The transmission curves of the filters used in our observations are shown in Figure 1.

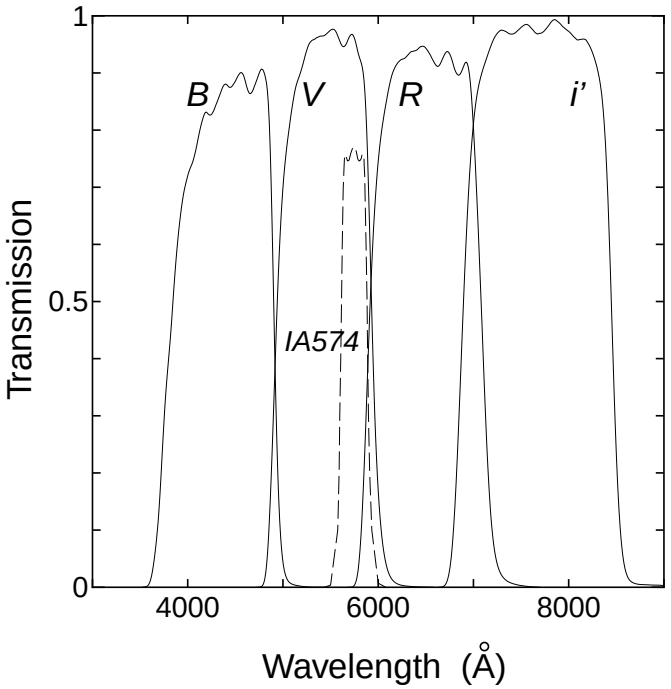

FIG. 1.—Transmission curves of the filters used in our observations

During the IA574-band observing run, only four CCD chips, each of which has 2048×4096 pixels, were installed in the Suprime-Cam. Two are MIT CCD chips, while the others are SITe chips; a northeast part ($13\farcm7 \times 13\farcm7$) of the broadband image was observed with the MIT chips and a northwest part ($13\farcm7 \times 13\farcm7$) was observed with the SITe chips. In this paper we present results obtained with the IA574 image taken with the SITe CCDs. The final sky coverage in our analysis is $10\farcm62 \times 12\farcm40$ in the $13\farcm7 \times 13\farcm7$ area covered by the SITe CCD chips. Our sky coverage is shown together with that of the broadband imaging (Ouchi et al. 2001) in Figure 2. Results obtained with the IA574 image with the MIT CCDs will be given in Yoshida et al. (2002). A journal of our all observations is summarized in Table 1.

The individual CCD data were reduced and combined using IRAF and the mosaic-CCD data reduction software developed by us (Yagi et al. 2002). The following photometric standard stars were observed to calibrate the data: (1) PG 0205+134 (Massey et al. 1988) and G158−100 (Oke 1990) for the August run, and (2) SA92, SA98, SA 95, SA101 (Landolt 1992), and SA95_42 (Oke 1990). The com-

TABLE 1
JOURNAL OF OBSERVATIONS

Band	Obs. Date	Total Integ. Time (s)	$m_{\rm lim}$(AB)[a]
B	2000 Nov 24, 25	10,620	27.6
V	2000 Nov 26, 27	4,800	26.4
R	2000 Aug 1	2,520	26.3
	2000 Nov 21–24	3,480	26.5
Total		6,000	26.7
i'	2000 Nov 25	2,700	26.2
IA574	2000 Aug 4	3,600	25.7

[a] The limiting magnitude (3 σ).

[14] Wide-field CCD cameras are also available on some 4 m class telescopes. One is the wide-field camera (a $36' \times 36'$ field of view) on the Kitt Peak National Observatory's 4 m Mayall telescope. Together with narrowband filters, this camera has been used to search for high-z Lyα emitters; the Large Area Lyα (LALA) survey (Rhoads et al. 2000; Rhoads & Malhotra 2001; MR02). The other is the Taurus Tunable Filter system on the 3.9 m AAT telescope (Bland-Hawthorn & Jones 1997; Baker et al. 2001). Although the current field of view is $\approx 10'$ in diameter, this tunable filter system will have a field of view of $\approx 30'$ in diameter if available on the prime focus of some 4 or 10 m class telescopes (Bland-Hawthorn et al. 2001).

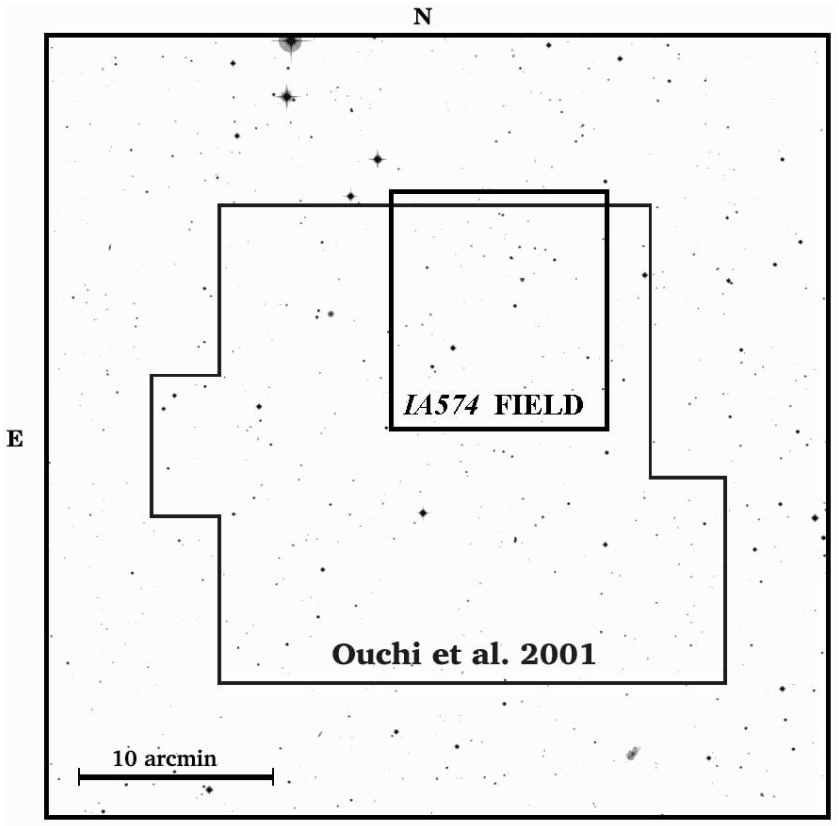

FIG. 2.—*Large box*: Subaru/XMM-Newton field covered by the broadband filters (Ouchi et al. 2001). *Small box*: Sky area covered with the IA574 filter. The background image is taken from the Palomar Observatory Sky Survey Digital Atlas.

bined images for the individual bands were aligned and smoothed with Gaussian kernels to match their seeing sizes. The final images cover a contiguous 618 arcmin^2 area with a point-spread function (PSF) FWHM of 0.″98 for the broadband data, and a 188 arcmin^2 area with a PSF FWHM of 0.″98 for the IA574 data. In the later analysis we use the 132 arcmin^2 area covered by both the IA574 and the broadband data. The final IA574 image is shown in Figure 3 together with a final color image made by using the broadband images.

The total size of the field is 10.′62 by 12.′40, corresponding to a total solid angle of ≈132 arcmin^2. The effective volume probed by the IA574 imaging has (comoving) transverse dimensions of 21.5 $h_{0.7}^{-1} \times 25.1\ h_{0.7}^{-1}$ Mpc, and the half-power points of the filter correspond to a comoving depth along the line of sight of 173.8 $h_{0.7}^{-1}$ Mpc ($z_{\rm min} \approx 3.60$ and $z_{\rm max} \approx 3.83$), where $h_{0.7} = H_0/(70\ {\rm km\ s^{-1}\ Mpc^{-1}})$. Therefore, a total volume of 93,952 $h_{0.7}^{-3}$ Mpc^3 is probed in our IA574 image, which is much wider than that of the previous pioneering studies, 10,410 $h_{0.7}^{-3}$ Mpc^3 (CH98) and 16,741 $h_{0.7}^{-3}$ Mpc^3 (S00) (see Table 6).

2.2. *Source Detection and Photometry*

Source detection and photometry were performed using SExtractor version 2.1.6 (Bertin & Arnouts 1996). Here we used the same source-detection criterion as that in Ouchi et al. (2001); a source must be a 5 pixel connection above 2 σ. The detection limit of the IA574 image is 25.7 mag for a 3 σ detection with a 2″ diameter aperture.

As for the source detection in the broadband images, the limiting magnitudes are $B = 27.6$, $V = 26.4$, $R = 26.7$, and $i' = 26.2$ for a 3 σ detection with a 2″ diameter aperture (Ouchi et al. 2001).

In the above source detection, we have detected ∼5500 sources down to IA574 = 26. In order to examine the completeness in the IA574 imaging, we show results of the number count as a function of IA574 magnitude in Figure 4. This figure shows that our source detection appears complete down to IA574 ≈ 25.4.

In order to make sure that our source selections were made with little ambiguity, we have newly performed a simulation using the IRAF ARTDATA (e.g., Kajisawa et al. 2000). We assume that galaxies have two types of light distributions, obeying (1) the de Vaucouleurs $r^{1/4}$ law and (2) the exponential law. For each type of galaxy we generated 300 model galaxies for each magnitude interval ($\Delta m = 0.2$ mag), i.e., 600 model galaxies in total. Their sky positions, half-light radius (1 to 7 kpc), and ellipticities are randomly determined. Then these model galaxies are put into the CCD data together with Poisson noises. After smoothing model-galaxy images to match to the seeing size, we try to detect them using SExtractor with the same procedure as that used in our paper. The detectability of the model galaxies in each band is shown in Figure 5 as a function of AB magnitude. As for objects brighter than IA574 = 25.4, we find that the detectability is higher than 50%. Therefore, we consider that this result appears to be consistent with the completeness limit, $m_{\rm lim}({\rm AB}) = 25.4$ shown in Figure 4 (see also the last column in Table 1).

The VR−IA574 color is plotted for the detected model galaxies with a color of VR−IA574 = 0 as a function of IA574 magnitude in Figure 6. It is shown that almost all the

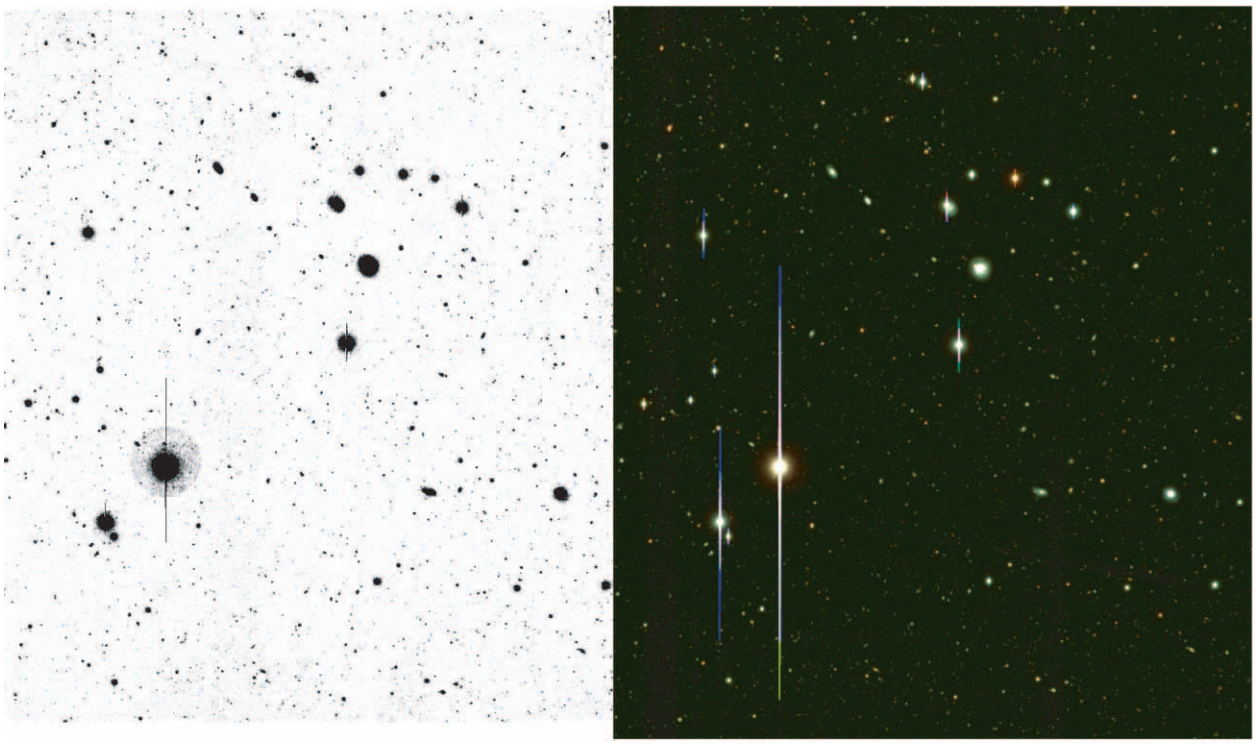

FIG. 3.—Final IA574 image (*left*) and the color image created by all the broadband images (*right*)

model galaxies are within 2 σ deviations. Therefore, we conclude that our source selections were done with appropriate accuracy for our purpose.

3. RESULTS

3.1. *Selection of IA574-Excess Objects*

Since the central wavelength of the V filter is bluer than that of the IA574 filter (5736 Å), we constructed an image that we will refer to as the "VR continuum," using a linear combination ($VR = 3.4V+1.0R$) of the deep V and R images after scaling them to the same photometric zero point; a 3 σ photometric limit of $VR \simeq 26.6$ in a 2″ diameter aperture. This enables us to more precisely sample the continuum at the same effective wavelength as that of the IA574 filter.

Although the detection limit of the IA574 image is 25.7, our source detection in IA574 appears complete down to ≈25.4 from Figure 4. Therefore, we tried to detect IA574-excess objects down to IA574 = 25.4 and made an IA574-selected catalog in which 3635 objects are contained. In Figure 7 we show the diagram between $VR-$IA574 and IA574 for the objects in the above catalog. Taking the scatter in the $VR-$IA574 color into account, we have selected strong emission-line sources with the criteria of $VR-\text{IA574} \geq 0.7$ and $\text{IA574} \leq 25.4$. These criteria are shown by the dotted lines in Figure 7. There are 101 sources that satisfy the above two criteria. We also show the distributions of 2 σ (*solid lines*) and 3 σ (*dashed lines*) errors in Figure 7. We remove 20 objects out of 101 sources because their $VR-$IA574 colors are smaller than the 2 σ error.

Since the central wavelength of the IA574 filter is closer to that of the V-band filter than to that of the R-band one, we adopted the criterion of $VR-\text{IA574} \geq 0.7$ as our primary criterion. However, red-color objects with a continuum break in the V-band window may also be detected as strong emission-line sources, even though they have little emission-line flux. In order to remove such objects, we also adopted another criterion, of $R-I\text{A574} \geq 0.7$. In Figure 8 we show the diagram between $VR-$IA574 and $R-$IA574 for the 81 objects found with the $VR-$IA574 color selection. As shown in this figure, 32 sources have been rejected because they do not show significant excess in the $R-$IA574 colors. Then we obtain a sample of 49 objects with both $VR-\text{IA574} \geq 0.7$ and $R-\text{IA574} \geq 0.7$. These color criteria mean that all the sources have their emission-line equivalent widths higher than 250 Å. It is also noted that dusty starburst galaxies with very red colors may not be found with our selection criteria, and thus the strong emission-line objects found in our search may be mostly either starburst galaxies with weak reddening or typical type 1 AGNs, such as quasars.

In order to ensure that our selection is reliable, we adopt another severe criterion: a source must be a 13 pixel connection above 2 σ. The reason for this is that a source under a ≈1″ seeing condition has a 13 pixel connection. Applying this criterion, we reject 24 sources among the 49 sources. Finally, we have made a careful visual inspection of all candidates' images in order to reject ambiguous objects that may be attributed to noises. In this procedure we rejected two sources because they show a linear or an unusual shape. Then we obtain our final sample of 23 emission-line sources.

We have also checked that none of our line-emitter candidates are either variable objects or moving objects by comparing the R-band image obtained in 2000 August with that from 2000 November. We do not find any spatially extended Lyα emitters like the Lyα blobs found by S00. On Lyα blobs, see Taniguchi & Shioya (2000) and Taniguchi, Shioya, & Kakazu (2001) and references therein.

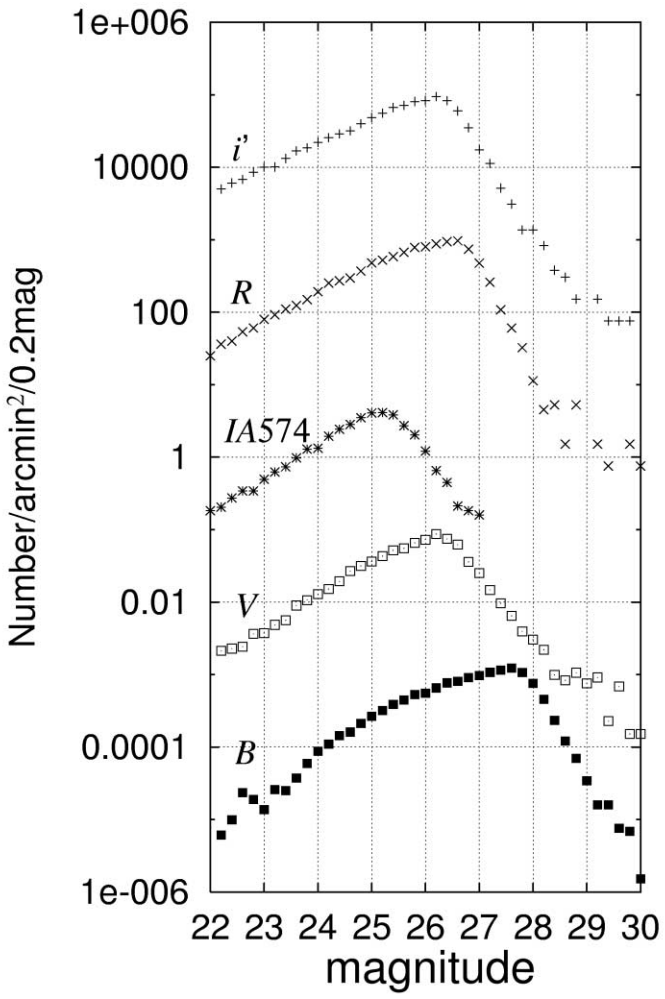

FIG. 4.—Number counts of sources found in our *B*, *V*, IA574, *R*, and *i'* images. The ordinates for *B*, *V*, *R*, and *i'* are multiplied by 10^{-4}, 10^{-2}, 10^{2}, and 10^{4}, respectively.

3.2. *Selection of IA574-Excess Objects at $z \approx 3.7$*

Our main aim in the present survey is to find strong Lyα emitters at $z \approx 3.7$. However, strong emission-line sources at lower redshift may be also found in our survey; e.g., C IV λ1550 sources at $z \approx 2.70$, Mg II λ2798 sources at $z \approx 1.05$, [O II] λ3727 sources at $z \approx 0.54$, Hβ λ 4861 at $z \approx 0.18$, [O III] λ5007 sources at $z \approx 0.15$, and so on. In order to distinguish Lyα emitters at $z \approx 3.7$ from emission-line objects at lower redshift, we investigate their broadband color properties. In this procedure we also take account of the observed emission-line equivalent widths.

First, we show that the $B-R$ color provides a nice tool to pick up Lyα emitters at $z \approx 3.7$. In Figure 9 we show the diagram of $B-R$ color as a function of redshift for galaxies with spectral energy distributions (SEDs) typical of E (the bulges of M31 and M81), Sbc, Scd, and Irr galaxies (Coleman, Wu, & Weedman 1980; hereafter CWW). The CWW SEDs cover a wavelength range from 1500 to 10000 Å. We therefore extend them below 1500 Å, assuming $f_\lambda \propto \lambda^{-0.82}$ (Kinney et al. 1993) down to 912 Å. As an SED of young starburst galaxies, we adopt an SED generated by the population synthesis model GISSEL96 (Bruzual & Charlot 1993); a galaxy with a constant star formation rate at an age of 10^8 yr. We also show expected redshift ranges for Lyα emitters at

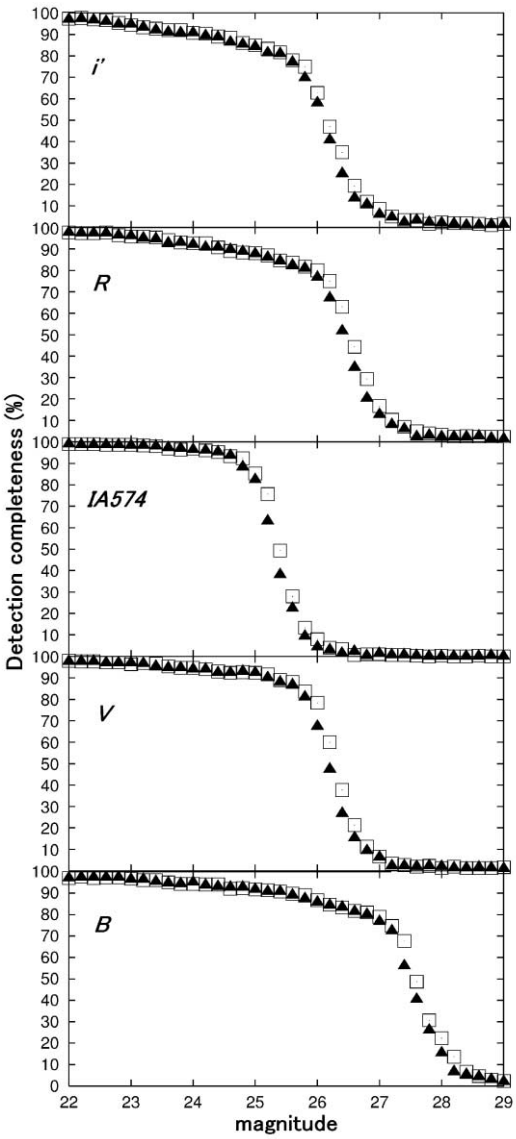

FIG. 5.—Detection completeness as a function of the apparent magnitude derived from the simulation (see text). Each symbol represents the adopted profiles of the artificial galaxies: de Vaucouleurs profile (*crosses*) and exponential profile (*plus signs*).

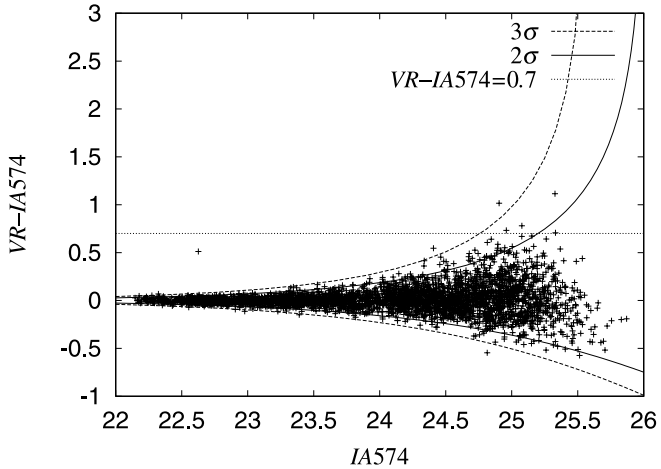

FIG. 6.—Distribution of the *VR*–IA574 color as a function of IA574 magnitude derived from the simulation (see text).

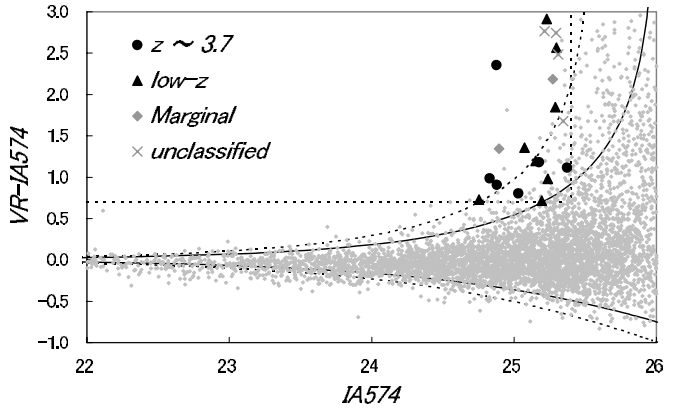

FIG. 7.—Objects detected to the apparent magnitude limit of IA574 = 26 in the IA574-selected catalog. The horizontal broken line corresponds to the color of $VR-\mathrm{IA574} = 0.7$. Objects above this line have strong emission lines, with $\mathrm{EW_{obs}} = 250$ Å or greater. Solid lines and dotted lines show the distribution of 2 σ and 3 σ error, respectively.

$z \approx 3.7$, [O II] λ3727 emitters at $z \approx 0.54$, and [O III] λ5007 emitters at $z \approx 0.15$.

For low-z galaxies, their $B-R$ colors are mainly determined by the stellar populations. On the other hand, for high-z galaxies beyond $z \sim 2.5$, their colors are mainly determined by the continuum depression due to the intergalactic extinction, i.e., cosmic transmission (e.g., Madau 1995). In Figure 9 we show three cases of different cosmic transmissions: (1) the mean value of the cosmic transmission by Madau (1995) (*solid curves*), (2) a value twice as large as the above mean value (*dotted lines*), and (3) a value half of the above mean value (*dashed lines*). These results imply that Lyα emitters at $z \approx 3.7$ have $B-R \gtrsim 1.0$ even if the cosmic transmission shows scatters within a factor of 2 from one line of sight to another.

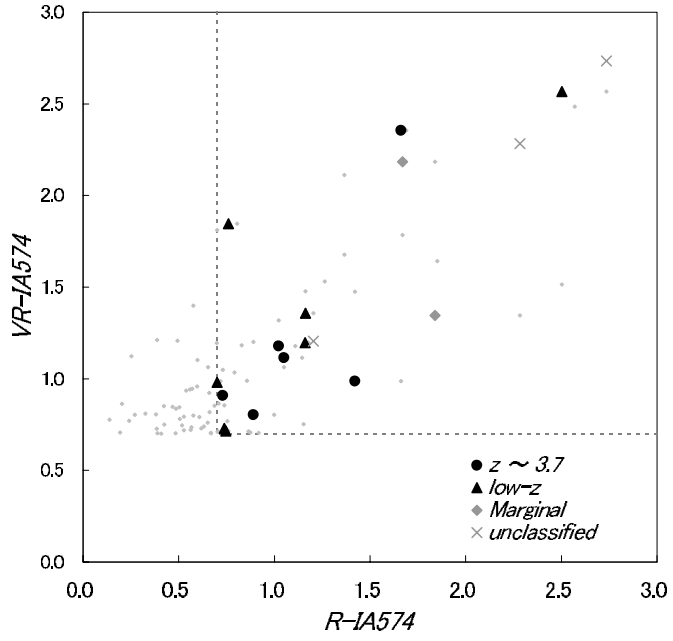

FIG. 8.—Plot of $VR-\mathrm{IA574}$ versus $R-\mathrm{IA574}$ for the 81 objects found with $VR-\mathrm{IA574} > 0.7$ and IA574 < 25.4 selection.

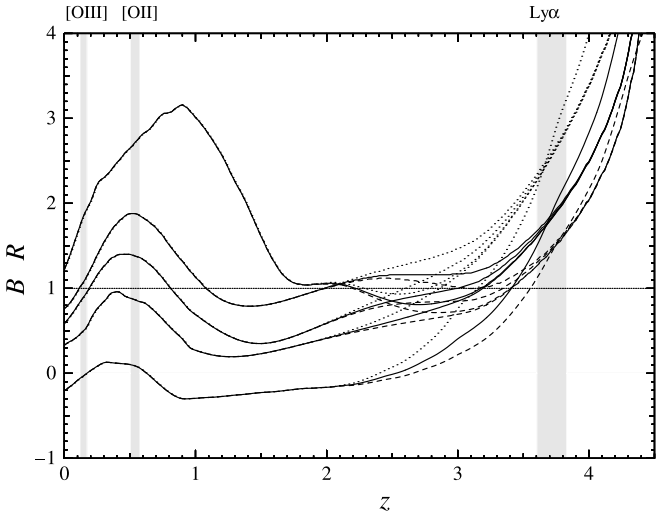

FIG. 9.—Diagram of $B-R$ color as a function of redshift for galaxies with spectral energy distributions (SEDs) typical of E, Sbc, Scd, and Irr (CWW). The bluest is young starburst model (see text). Redshift ranges for Lyα emitters at $z \approx 3.7$, [O II] λ3727 emitters at $z \approx 0.53$, and [O III] λ5007 emitters at $z \approx 0.15$ are also shown by shaded strips.

It is also expected that E-, Sbc-, and Scd-type galaxies at lower redshift have $B-R > 1$. However, our strong emission-line objects found in this study have large emission-line equivalent widths; i.e., $\mathrm{EW_{obs}} \geq 250$ Å. This value corresponds to a rest-frame equivalent width of $\mathrm{EW_0} = 163$ Å for [O II] λ3727 emitters at $z \approx 0.54$, $\mathrm{EW_0} = 212$Å for Hβ emitters at $z \approx 0.18$, and $\mathrm{EW_0} = 217$ Å for [O III] λ5007 emitters at $z \approx 0.15$. Since it is known that typical rest-frame [O II] or [O III] emission-line galaxies in the nearby universe have $\mathrm{EW_0} < 100$ Å (e.g., Jansen et al. 2000), it is unlikely that the strong emission-line sources with $B-R \geq 1.0$ are low-z sources (see also § 3.3).

Second, we show the diagram between $B-R$ and $R-i'$ for all the objects detected in the broadband B, R, and i' images in the right panel of Figure 10. We also show color evolutions of model galaxies with the CWW SEDs typical of E, Sbc, Scd, and Irr galaxies and with the SED for young starburst galaxies as a function of redshift (*left*). The model results show that Lyα emitters at $z \sim 3.7$ may occupy the shaded domain defined with both $B-R > 1.0$ and $R-i' \lesssim 0.7$, although the latter color constraint appears not so strong. This figure also implies once again that either strong [O II] or [O III] emitters could have $B-R < 1$.

It seems necessary to examine whether or not strong C IV emitters (i.e., quasars) at $z \approx 2.7$ are misclassified as Lyα emitters at $z \approx 3.7$. Using the composite spectrum of SDSS quasars (Vanden Berk et al. 2001), we estimate the $B-R$ color when we observe a quasar with the SDSS composite spectrum at $z \approx 2.7$. We find that its $B-R$ color is much bluer than 1.0 because the Lyman break comes shorter than the B-band transmission. Therefore there is no possibility of selecting quasars at $z \approx 2.7$ when we use the above color criteria.

In conclusion, one can identify Lyα emitters at $z \approx 3.7$ using the two color criteria: (1) $B-R \geq 1.0$, and (2) $R-i' \leq 0.7$. It is again noted that the observed larger emission-line equivalent widths (i.e., $\mathrm{EW_{obs}} \geq 250$ Å) allow us to adopt the above simple color criteria in our selection. In this

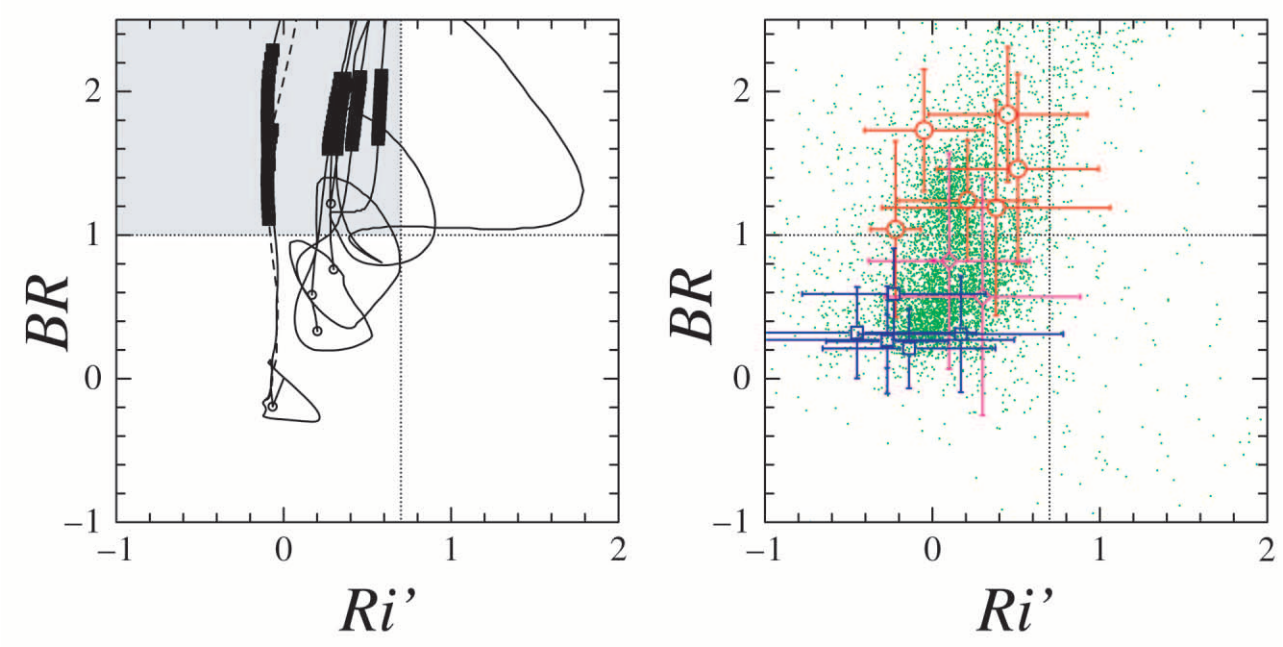

FIG. 10.—Diagram of objects in the IA574-selected catalog between $B-R$ and $R-i'$ (*right*). Candidates of Lyα emitters at $z \approx 3.7$ are located in the domain defined with the two color criteria: (1) $B-R \geq 1.0$, and (2) $R-i' \leq 0.7$. Our final candidates of Lyα emitters at $z \sim 3.7$ are shown by red open circles. On the other hand, our final low-z emitters are shown by blue open squares which have $B-R < 1.0$. The marginal Lyα emitter-candidates are shown by pink open diamonds. In the left panel, we show the model predictions for the mean cosmic transmission (*solid lines*; see text). For the model of young starburst galaxies we also show the case in which the value of the effective optical depth is a half the mean value (*dashed line*). The loci of model galaxies in the redshift between 3.6 and 3.83 are shown in thick lines. Open circles show model galaxies at $z = 0$.

way, we have classified our 23 emission-line sources into the following four categories.

1. Lyα emitters at $z \approx 3.7$: Six emission-line objects satisfy the above two criteria, and thus they are identified as Lyα emitters at $z \approx 3.7$, which are marked by open red circles in the upper shaded region in Figure 10. Their positions, emission-line equivalent widths, and photometric properties are given in Table 2. In Figure 11, we show the B, V, IA574, R, and i' images of each object in our sample of Lyα emitters at $z \approx 3.7$. The SED is also shown in the right panel for each object. We note that one object (No. 4) appears to be extended in the IA574 image. Its angular diameter (above 2 σ) is estimated as $2''.0$, corresponding to the linear diameter of 14.3 $h_{0.7}^{-1}$ kpc at $z = 3.7$. Although we cannot rule out the possibility that this source is a low-z object, we do not adopt any criterion on the source size in our source selection procedure. Therefore we include this source as a Lyα-emitter candidate.

2. Marginal Lyα emitters at $z \approx 3.7$: Two objects, shown by pink colors in Figure 10, appear marginal between objects at $z \approx 3.7$ and ones at lower redshift, because their $B-R$ colors marginally satisfy the condition of $B-R \geq 1.0$ if their observational errors are taken into account. Therefore we call them "marginal" Lyα emitters at $z \approx 3.7$. Their positions, emission-line equivalent widths, and photometric properties are given in Table 3. In Figure 12 we show the B, V, IA574, R, and i' images of each object in our sample of marginal Lyα emitters at $z \approx 3.7$. The SED is also shown in the right panel for each object.

3. Low-z emission-line objects: Eight objects among the remaining 15, which are marked by open squares in Figure 10, may be emission-line objects at lower redshifts, because their $B-R$ colors are significantly bluer than 1.0. Their positions, emission-line equivalent widths, and photometric properties are given in Table 4. In Figure 13 we show the B, V, IA574, R, and i' images of each object in our sample of low-z emitter candidates. The SED is also shown in the right panel for each object.

TABLE 2
PHOTOMETRIC PROPERTIES OF LYα-EMITTER CANDIDATES AT $z \approx 3.7$

No.	α(J2000.0)	δ(J2000.0)	EW_{obs} (Å)	B	V	IA574	R	i'	VR	VR−IA574	R−IA574	$B-R$	$R-i'$
1.....	2 17 54.90	−5 09 13.7	1014 ± 439	27.73	26.35	24.88	26.54	26.16	>27.02	>2.14	1.66	1.19	0.38
2.....	2 17 34.30	−5 09 35.9	454 ± 273	27.46	26.54	25.37	26.42	26.64	26.49	1.11	1.05	1.04	−0.22
3.....	2 17 37.87	−5 00 11.7	439 ± 220	28.04	26.45	25.18	26.20	25.75	26.35	1.18	1.02	1.84	0.45
4.....	2 17 46.26	−5 11 42.5	414 ± 159	27.71	25.76	24.83	26.25	25.74	25.81	0.99	1.42	1.46	0.51
5.....	2 17 38.09	−5 11 20.0	307 ± 149	27.16	25.84	25.03	25.92	25.71	25.84	0.80	0.89	1.24	0.21
6.....	2 18 06.71	−5 10 05.5	269 ± 115	27.34	25.88	24.88	25.61	25.66	25.79	0.91	0.73	1.73	−0.05

NOTE.—Units of right ascension are hours, minutes, and seconds, and units of declination are degrees, arcminutes, and arcseconds.

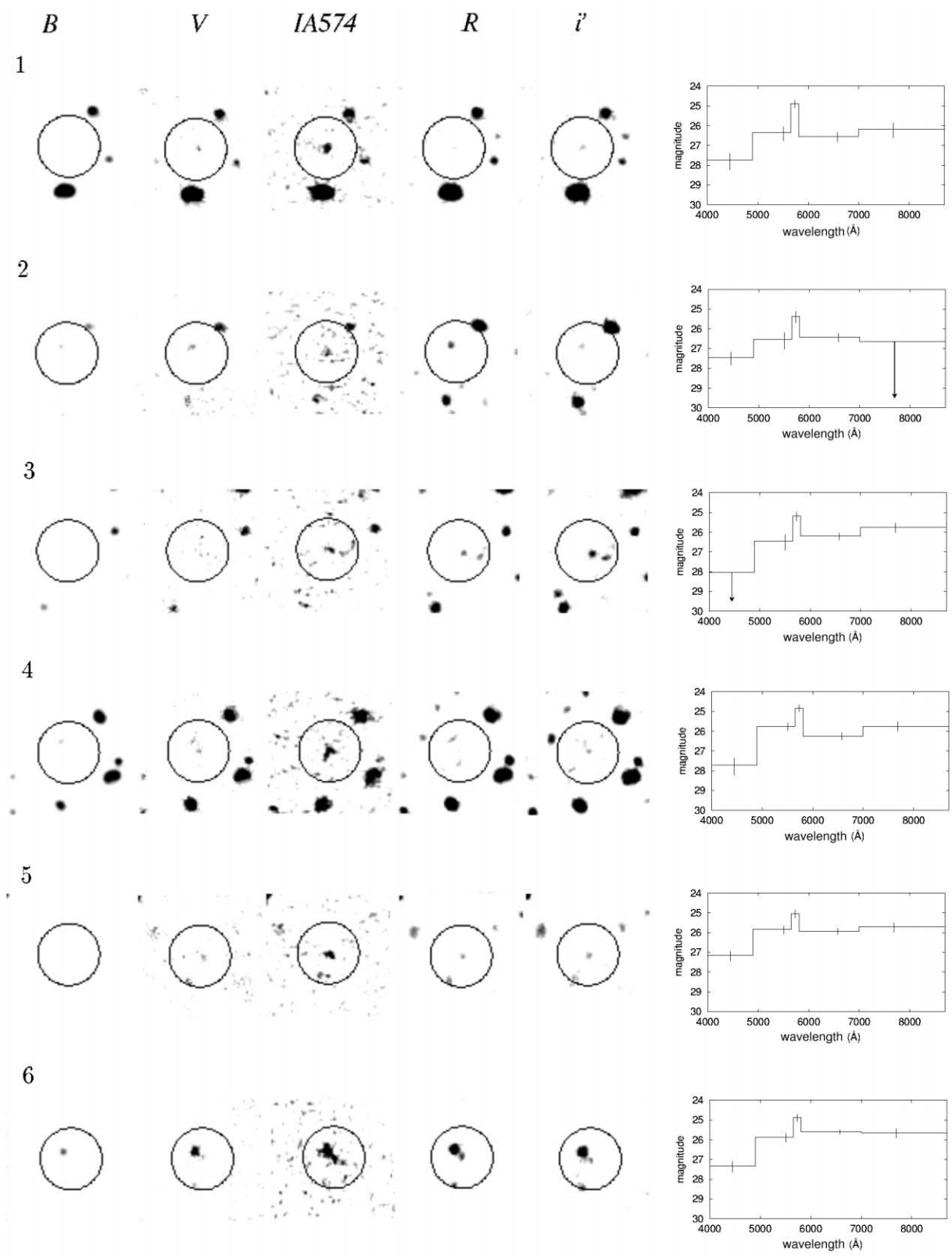

FIG. 11.—Broadband and IA574 images of the most probable candidates of Lyα emitters at $z \approx 3.7$. Each box is 16″ on a side. Each circle has a 4″ radius. The SED is also shown in the right panel for each object.

TABLE 3
PHOTOMETRIC PROPERTIES OF MARGINAL Lyα-EMITTER CANDIDATES

No.	α(J2000.0)	δ(J2000.0)	EW_{obs} (Å)	*B*	*V*	IA574	*R*	*i'*	*VR*	*VR*–IA574	*R*–IA574	*B*–*R*	*R*–*i'*
1.....	2 17 43.48	−5 07 02.9	1022 ± 635	27.51	26.84	25.27	26.94	26.64	>27.02	>1.75	1.67	0.57	0.30
2.....	2 17 54.10	−5 07 54.5	687 ± 287	27.56	26.17	24.90	26.74	>26.64	26.24	1.35	1.84	0.83	<0.10

TABLE 4
PHOTOMETRIC PROPERTIES OF LOW-*z* EMITTER CANDIDATES

No.	α(J2000.0)	δ(J2000.0)	EW_{obs} (Å)	*B*	*V*	IA574	*R*	*i'*	*VR*	*VR*–IA574	*R*–IA574	*B*–*R*	*R*–*i'*
1.....	2 17 25.93	−5 04 30.4	>1177	27.75	>26.84	25.23	>27.12	>26.64	>27.02	>1.79	>1.89	<0.63	...
2.....	2 17 57.87	−5 11 43.5	>1091	27.52	>26.84	25.30	>27.12	>26.64	>27.02	>1.72	>1.82	<0.40	...
3.....	2 17 51.99	−5 09 05.0	536 ± 244	26.51	26.57	25.07	26.24	26.51	26.43	1.36	1.16	0.28	−0.27
4.....	2 17 51.77	−5 08 01.8	535 ± 261	26.62	26.41	25.15	26.31	26.14	26.35	1.20	1.16	0.30	0.17
5.....	2 17 38.24	−5 09 14.8	284 ± 173	26.37	>26.84	25.29	26.05	26.50	>27.02	>1.73	0.76	0.32	−0.45
6.....	2 17 54.42	−5 08 23.9	268 ± 105	25.75	25.50	24.75	25.49	25.76	25.48	0.73	0.74	0.26	−0.27
7.....	2 17 28.61	−5 08 54.1	261 ± 154	26.53	25.96	25.19	25.94	26.17	25.91	0.71	0.75	0.59	−0.23
8.....	2 17 51.73	−5 00 54.9	254 ± 153	26.15	26.32	25.24	25.94	26.08	26.22	0.98	0.70	0.21	−0.14

4. Unclassified emission-line objects: Six objects out of the remaining seven are detected only in the IA574. Therefore we cannot use their broadband photometric properties, and they are left as "unclassified" emission-line objects. The last one is detected only in the *R* band, except for IA574. Their positions, emission-line equivalent widths, and photometric properties are given in Table 5. In Figure 14 we show the *B*, *V*, IA574, *R*, and *i'* images of each object. The SED is also shown in the right panel for each object.

3.3. *Equivalent Widths of Emission Features*

First, we investigate the emission-line equivalent width of the low-*z* emission-line sources. We show the rest-frame [O II] and [O III] emission-line equivalent widths (*crosses*) as a function of *B*−*R* in Figures 15 and 16, respectively. Note that we use the *B*−*R* color in the Vega-based photometric system, $(B-R)_{Vega}$ (e.g., Fukugita, Shimasaku, & Ichikawa 1995) in order to compare the observations with model results, which are obtained by using the population synthesis model GISSEL96 (Bruzual & Charlot 1993). In our model calculations we use the τ model with both $\tau = 1$ Gyr and the metallicity of $Z = 0.02$. Model results for the $(B-R)_{Vega}$ are obtained for the following ages: 10, 100, 500 Myr, 1, 2, 3, 4, 7, and 10 Gyr. For each model we derive the Hβ luminosity from the Lyman continuum luminosity using the following formula (Leitherer & Heckman 1995),

$$L(\mathrm{H}\beta) = 4.76 \times 10^{-13} N(\mathrm{H}^0) \text{ ergs s}^{-1} , \quad (1)$$

where $N(H^0)$ is the number density of Lyman continuum

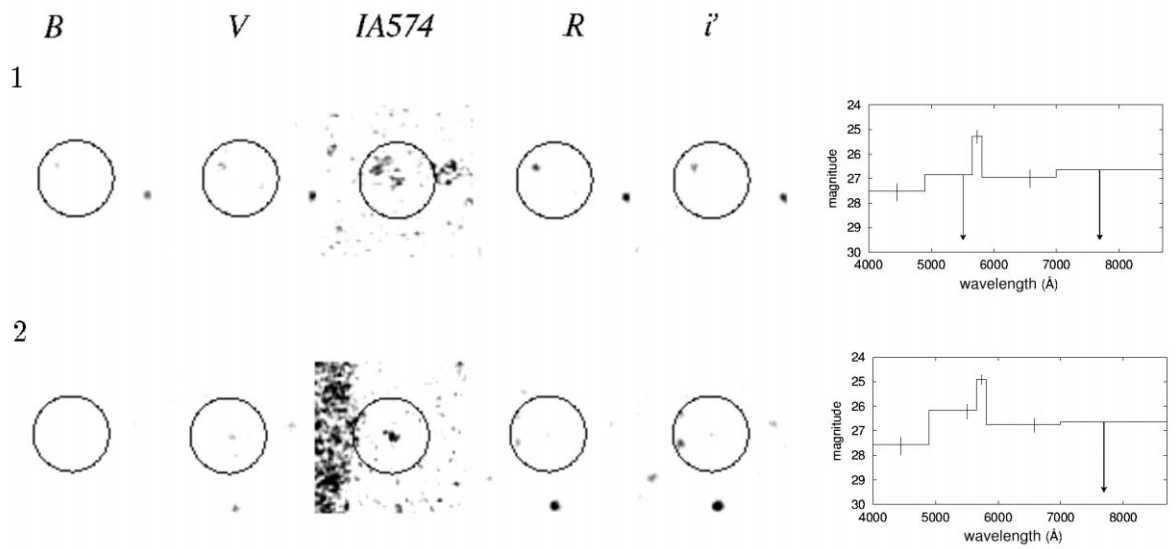

FIG. 12.—Broadband and IA574 images of emitter candidates classified as "marginal" (see text). Each box is 16″ on a side. Each circle has a 4″ radius. The SED is also shown in right panel for each object.

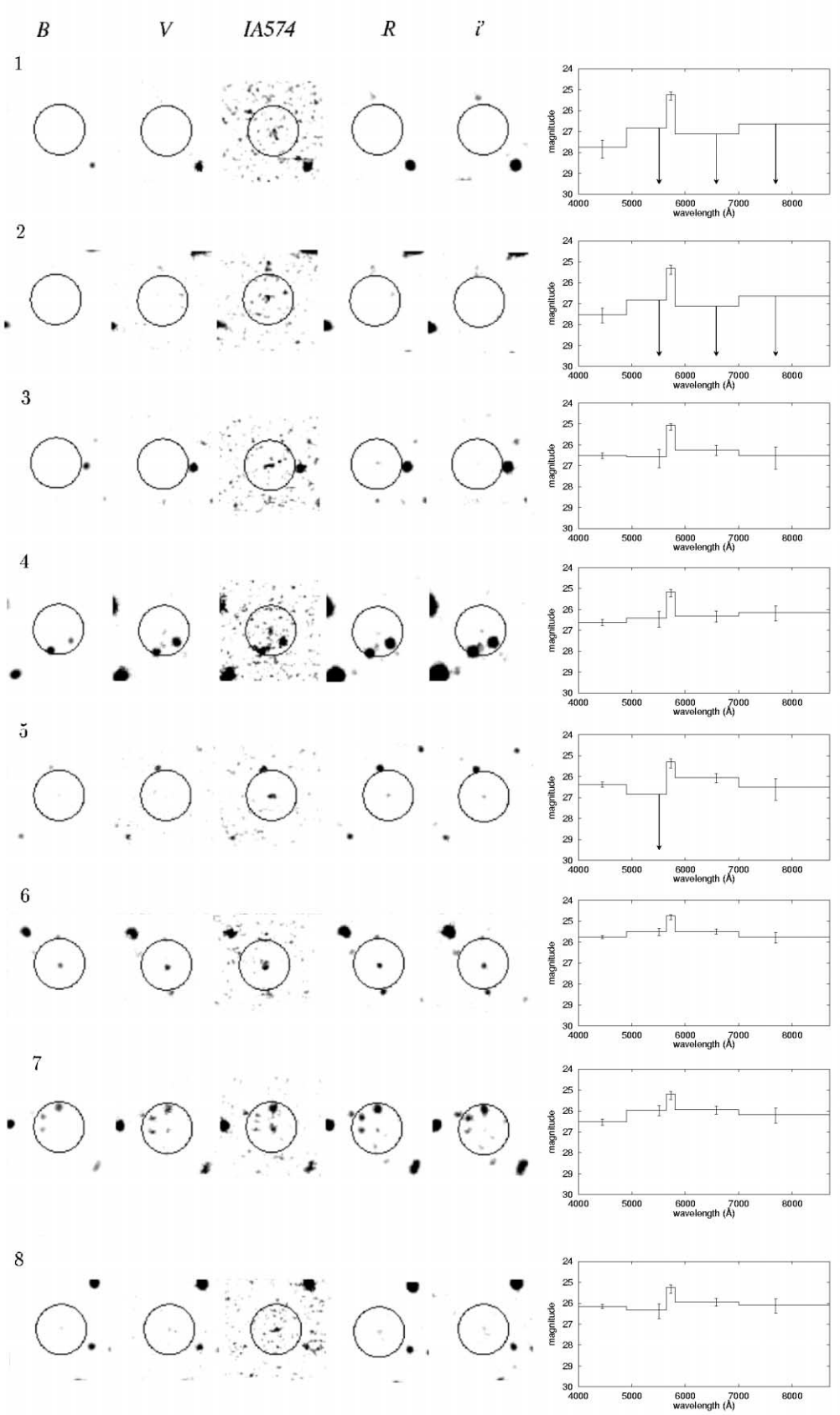

FIG. 13.—Broadband and IA574 images of the most probable candidates of Lyα emitters at lower redshifts. Each box is 16″ on a side. Each circle has a 4″ radius. The SED is also shown in right panel for each object.

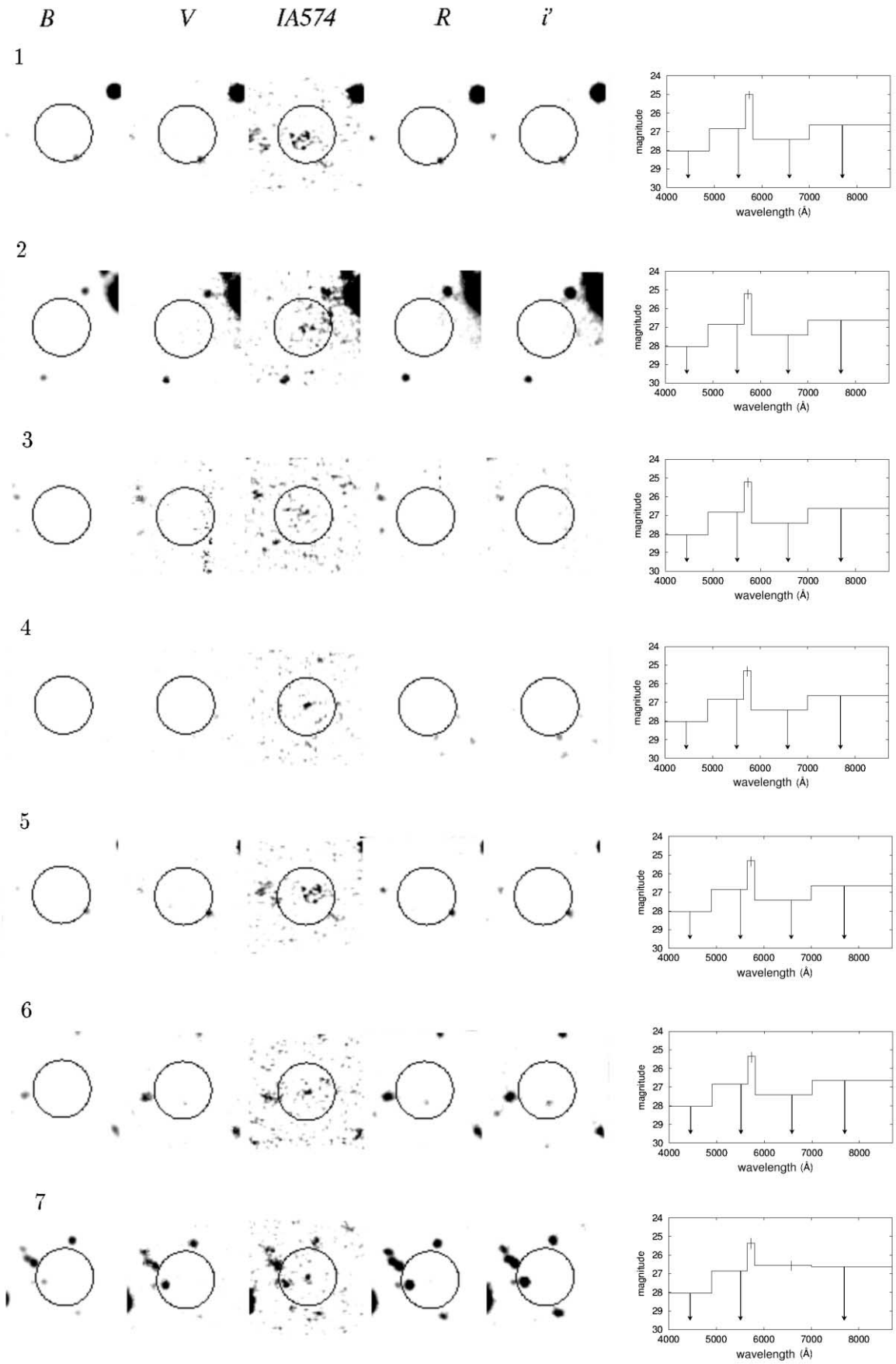

FIG. 14.—Broadband and IA574 images of the unclassified emission-line source which is detected only in the IA574 image. Each box is 16″ on a side. Each circle has a 4″ radius. Its SED is also shown in right panel.

TABLE 5
PHOTOMETRIC PROPERTIES OF UNCLASSIFIED EMITTER CANDIDATES

No.	α(J2000.0)	δ(J2000.0)	EW_{obs} (Å)	B	V	IA574	R	i'	VR	VR–IA574	R–IA574	$B-R$	$R-i'$
1.....	2 17 43.08	−5 07 01.2	>1508	>28.04	>26.84	25.01	>27.12	>26.64	>27.02	>2.01	>2.11	...	...
2.....	2 17 39.25	−5 08 27.3	>1199	>28.04	>26.84	25.21	>27.12	>26.64	>27.02	>1.81	>1.91	...	...
3.....	2 17 57.10	−5 12 22.2	>1092	>28.04	>26.84	25.30	>27.12	>26.64	>27.02	>1.73	>1.82	...	...
4.....	2 17 26.82	−5 01 12.4	>1080	>28.04	>26.84	25.31	>27.12	>26.64	>27.02	>1.72	>1.81	...	...
5.....	2 17 43.20	−5 07 02.3	>1074	>28.04	>26.84	25.31	>27.12	>26.64	>27.02	>1.71	>1.81	...	...
6.....	2 17 52.84	−5 09 50.4	>1008	>28.04	>26.84	25.36	>27.12	>26.64	>27.02	>1.66	>1.75	...	...
7.....	2 17 42.91	−5 11 09.3	569 ± 332	>28.04	>26.84	25.35	26.55	>26.64	>27.02	>1.67	1.20	>1.49	<−0.09

photon per second. The equivalent widths of [O II] and [O III] emission are estimated for the following cases: (1) $\log$ [O II]/H$\beta = 0$ (*lower solid line*, Fig. 15) and 0.5 (*upper solid line*, Fig. 15), and (2) $\log$ [O III]/H$\beta = -0.5$ (*lower solid line* Fig. 16) and 0.5 (*upper solid line*, Fig. 16). The low-z emission-line candidates found in our survey appear to show much stronger emission-line galaxies than do star-forming galaxies found in the local universe. Such examples have indeed been found by Ohyama et al. (1999); e.g., [O II] emitters at $z \sim 0.5$ have $EW_{obs} \sim 200$ Å. Such galaxies must be very blue, and thus their $B-R$ colors are expected to be much bluer than $B-R = 1$ (see also Stockton & Ridgeway 1998; Stern et al. 2000). These results also reinforce the conclusion that low-z strong emission-line galaxies do not have $B-R > 1$.

Second, we compare the distribution of observed emission-line equivalent widths (EW_{obs}) among the four samples in Figure 17: (1) the Lyα-emitter sample, (2) the marginal Lyα-emitter sample, (3) the low-z-emitter sample, and (4) the unclassified sample. We obtain the average equivalent widths of 482 ± 246 Å for the Lyα-emitter sample. If we combine the Lyα-emitter sample and the marginal ones, we obtain the average equivalent widths of 575 ± 280 Å. On the other hand, we obtain the average equivalent widths of for the low-z sample, which is smaller than the above values. This makes sense because the EW_{obs} of the Lyα-emitter candidates is amplified by a factor of $\approx$4.7, while the amplification factor must be rather small for the low-z-emitter candidates; e.g., a factor of 1.54 for [O II] emitters.

Finally, it is interesting to note again that the low-z emitters detected in our survey may have large rest-frame emission-line equivalent widths; e.g., $EW_0 \sim 150$–200 Å if they are either [O II], Hβ, or [O III] emitters. As noted before, it is known that typical rest-frame [O II] or [O III] emission-line galaxies in the nearby universe have $EW_0 < 100$ Å (e.g., Jansen et al. 2000). If emission-line galaxies are located at $z \approx 0.151$–0.174, both Hβ and [O III] $\lambda\lambda$4959, 5007 emission lines can be detected simultaneously in our IA574 image, resulting in larger than normal emission-line equivalent widths. However, it seems unlikely that most of the low-z emitters are located at the above narrow redshift range. Furthermore, Ohyama et al. (1999) found very strong [O II] emitters at $z \approx 0.5$ serendipitously. In Figure 18 we show a diagram between EW_{obs} and VR for the eight low-z emitters. It appears that fainter galaxies tend to have larger EW_{obs}. Therefore, it is suggested that a number of emission-line galaxies with large equivalent widths may have not yet

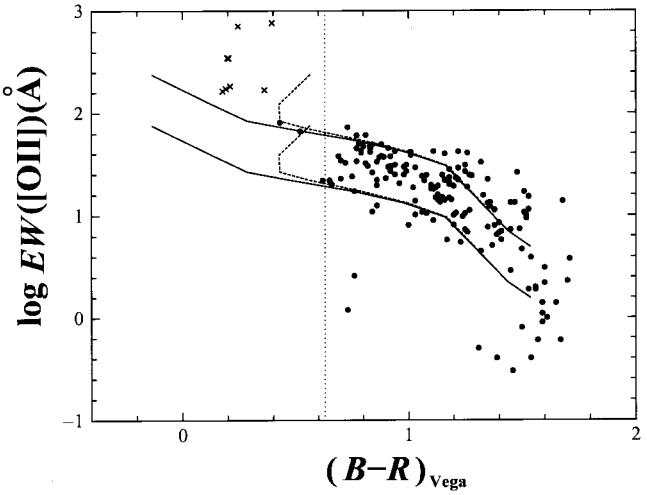

FIG. 15.—Diagram of log EW([O II]) as a function of $B-R$. The data of the low-z emitter candidates in our survey are shown by crosses. The observational data of nearby galaxies (*dots*) are taken from Jansen et al. (2000). Solid lines show our model predictions, using the population synthesis model GISSEL96 (Bruzual & Charlot 1993), with the star-formation timescale of 1 Gyr and ages of 10 (reddest), 7, 4, 3, 2, 1, 0.5, 0.1, and 0.01 (bluest) Gyr. We assume that $L(\mathrm{H}\beta) = 4.76 \times 10^{-13} N(\mathrm{H}^0)$(ergs s^{-1}), where $N(\mathrm{H}^0)$ is a ionizing photon production rate in units of s^{-1}, and $\log$ [O II]/H$\beta = 0.0$ (*lower solid line*) and 0.5 (*upper solid line*). When emission-line flux is also taken into account in the R magnitude, the solid lines are shifted to the dashed lines. The dotted vertical line shows a typical color of an Irr galaxy.

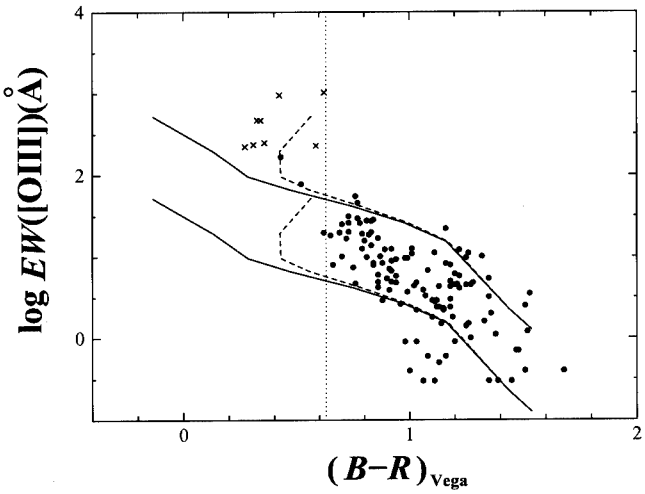

FIG. 16.—Diagram of log EW([O III]) as a function of $B-R$. The data of the low-z emitter candidates in our survey are shown by crosses. The observational data (*dots*) are taken from Jansen et al. (2000). The dotted vertical line shows a typical color of an Irr galaxy. The meanings of solid and dashed lines are the same as those in Fig. 15.

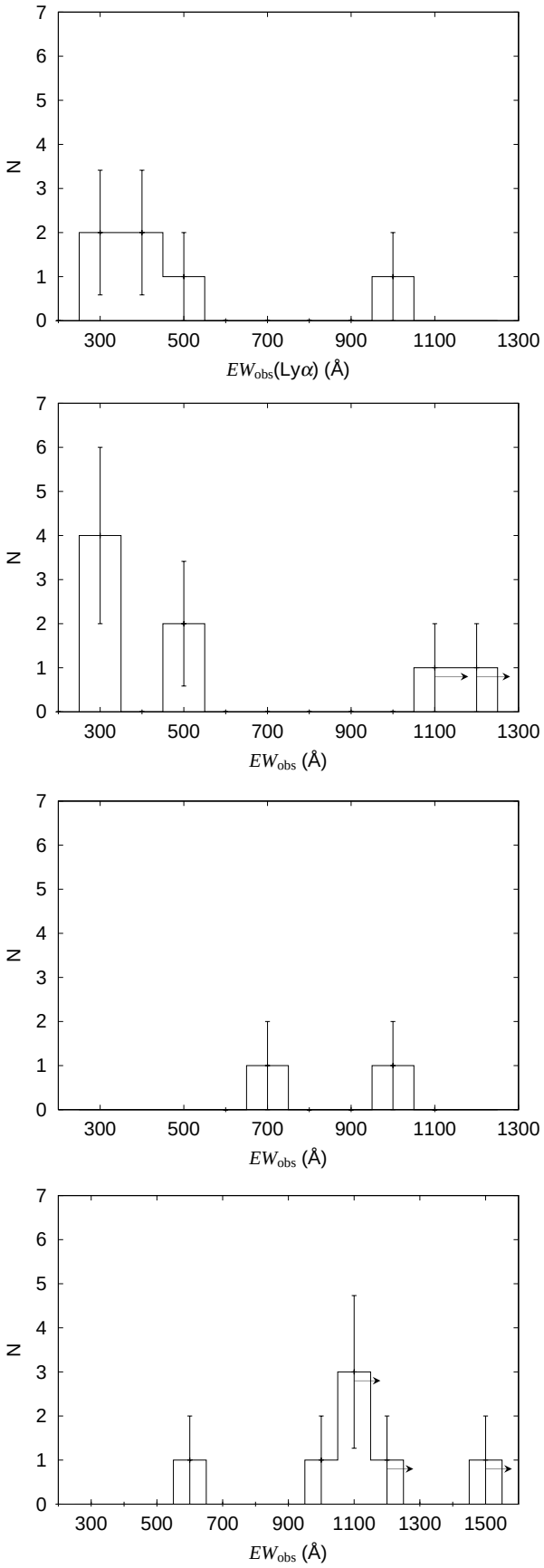

FIG. 17.—Comparison of histograms of EW_{obs}(Lyα) between the six Lyα-emitter candidates at $z \approx 3.7$ (*top*) and eight low-z emitters (*second from top*), two marginal emitter candidates (*third from top*), and seven unclassified emitter candidates (*bottom*).

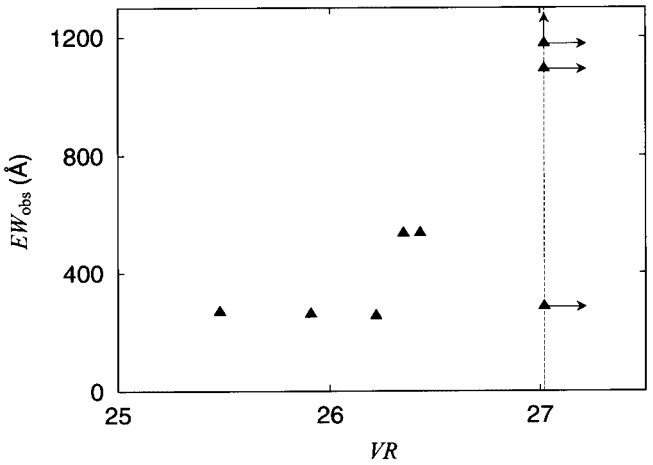

FIG. 18.—Diagram between EW_{obs} and VR for the eight low–z-emitter candidates.

been probed in previous surveys because they are too faint to be included in bright magnitude-limited samples.

3.4. *Spatial Distribution of the IA574-Excess Objects*

We investigate the spatial distributions of the Lyα-emitter candidates at $z \approx 3.7$. In Figure 19 we plot the spatial distributions for the four emitter samples. The Lyα-emitter candidates at $z \approx 3.7$ are shown by open circles. Five among the six candidates, together with the two marginal Lyα-emitter candidates, are distributed in the southern part of our image. However, the low-z emitter sample also shows such a tendency. We do not discuss this issue in further detail because our survey depth is not so deep and spectroscopic confirmation has not yet been done.

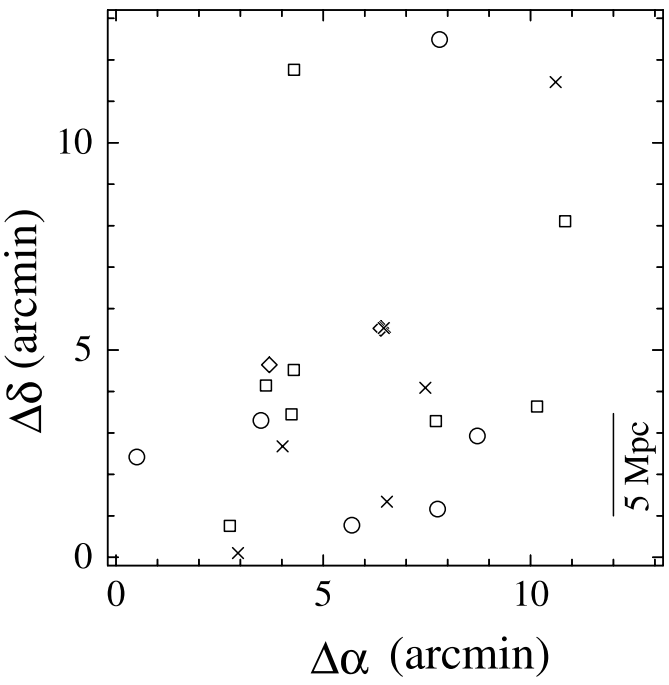

FIG. 19.—Celestial positions of the six Lyα-emitter candidates at $z \approx 3.7$ (*open circles*), marginal emitter candidates (*open diamonds*), eight low-z emitter candidates (*open squares*), and seven unclassified emitter candidates (*crosses*).

4. DISCUSSION

4.1. *Nature of the Lyα-Emitter Candidates at $z \approx 3.7$*

We have detected six Lyα emitters and two marginal candidate emitters at $z \approx 3.7$. Although it is uncertain whether they are genuine star-forming galaxies or active galactic nuclei, it is highly probable that the emission feature is attributed to Lyα emission, and thus their redshifts are $z \approx 3.7$. Therefore it seems interesting to investigate their rest-frame Lyα equivalent widths EW_0(Lyα) (see Table 7). We note that, because of the effect of cosmic transmission, the value of EW_0(Lyα) evaluated here is smaller than the intrinsic value (see the Appendix). In Figure 20 we show a histogram of EW_0(Lyα) for the six sources. It is shown that the rest-frame equivalent widths range from 57 to 216 Å. The average value is $\langle EW_0(\mathrm{Ly}\alpha)\rangle \simeq 103 \pm 53$ Å. These values are comparable to those found by CH98 and S00 (except the two Lyα blobs found by S00). It is noted that Vanden Berk et al. (2001) obtained $\langle EW_0(\mathrm{Ly}\alpha)\rangle \simeq 93 \pm 0.7$ Å for a sample of over 220 quasars found in the Sloan Digital Sky Survey. This median value is also similar to the median value obtained for our sample.

In Figure 21 we compare our result with those of the previous narrowband surveys by CH98, S00, and Malhorta & Rhoads (2002, hereafter MR02). Since their survey volumes are different from ours, we have reevaluated the frequency distributions of the equivalent widths so as to match to our survey volume. For the results by MR02 we adopt the frequency distribution in which 1 σ R-band continuum is used in the estimate of equivalent widths. As shown in this figure, all the previous surveys have detected more numerous Lyα emitters by a factor of 3 to 9 than our survey for objects with $EW_0 = 50$ to 100 Å. The reason for this seems that their survey depths in EW are deeper than that of our survey.

Both our survey and the LALA survey by MR02 succeeded in detecting stronger Lyα emitters with $EW_0 > 100$ Å. Since it is considered that such strong emitters may be rarer than weak emitters in general, their wide-field coverages enable them to detect such strong emitters. We also note that the LALA survey detected more numerous sources whose equivalent widths reach ~500 Å. This is because their survey depths in flux are deeper than ours.

In Figure 22 we show a diagram of EW_0(Lyα) versus VR magnitude for the six sources. It is found that the fainter objects tend to have larger EW_0(Lyα). This tendency can be understood in terms of the so-called Baldwin effect (Baldwin 1977) for active galactic nuclei. However, it is also known that such tendency can be found in star-forming galaxies (e.g., Cowie et al. 1996), although the correlation shows much larger scatter than that for active galactic nuclei. Since the correlation shown in Figure 22 exhibits the large scatter, it is suggested that the majority of the detected Lyα emitters are star-forming galaxies like those found by CH98 and S00, rather than quasars.

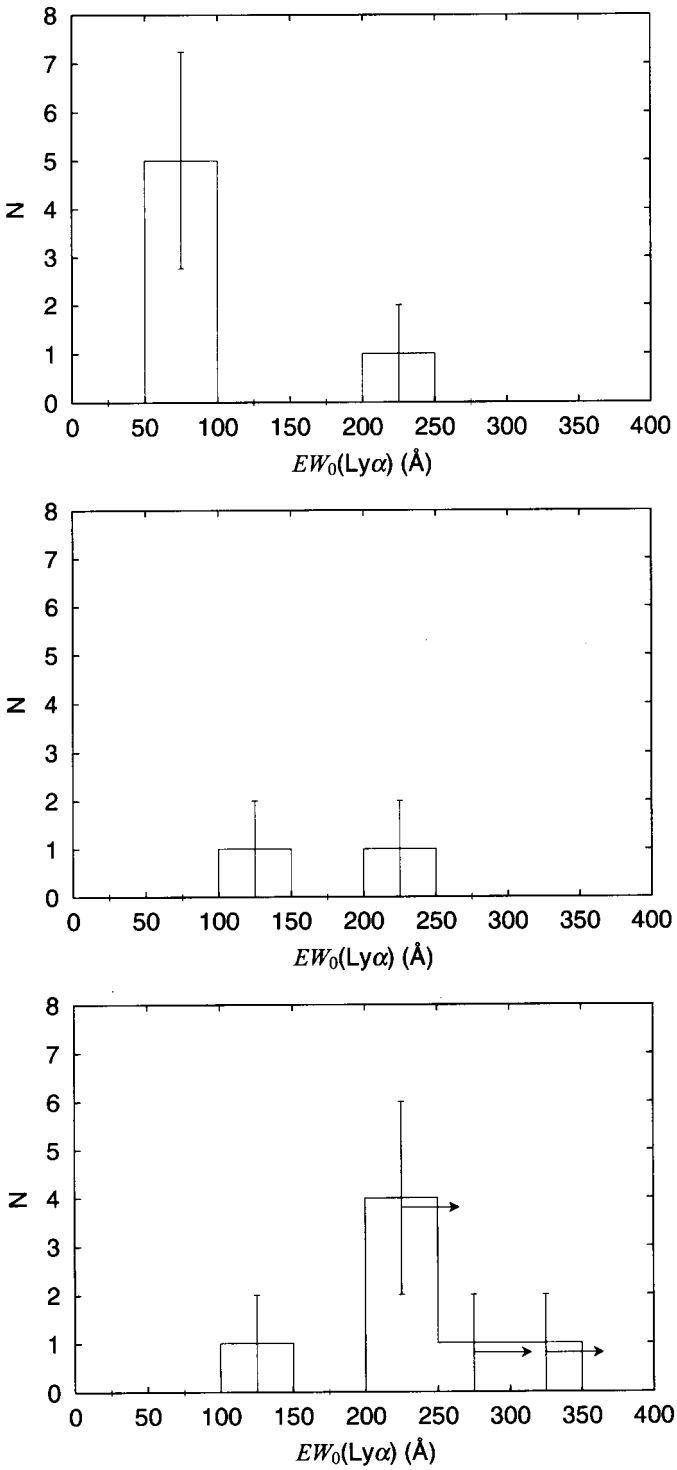

FIG. 20.—Frequency distribution of EW_0(Lyα) for the six Lyα-emitter candidates at $z \approx 3.7$ (*top*), the two marginal emitter candidates (*middle*), and the seven unclassified emitter candidates (*bottom*).

4.2. *Space Density of the Lyα emitters at $z \approx 3.7$*

We have detected the six candidates of Lyα emitters at $z \approx 3.7$ in a volume of 93,952 Mpc^3. This yields a space density of Lyα emitters, $n(\mathrm{Ly}\alpha) \simeq 6.4 \times 10^{-5}$ Mpc^{-3}. CH98 obtained $n(\mathrm{Ly}\alpha) \simeq 9.6 \times 10^{-4}$ Mpc^{-3} for the Hubble Deep Field and $n(\mathrm{Ly}\alpha) \simeq 1.3 \times 10^{-3}$ Mpc^{-3} for the SSA22 field. S00 obtained $n(\mathrm{Ly}\alpha) \simeq 4.3 \times 10^{-3}$ Mpc^{-3} for the Lyman break galaxies (LBG) overdensity region. Further, K00 obtained $n(\mathrm{Ly}\alpha) \simeq 1.3 \times 10^{-3}$ Mpc^{-3} in their La Palma field (Mendez et al. 1997). The density we obtained is lower by 1 order of magnitude than their values. This difference may be partly due to the fact that their survey depths are deeper by a factor of 3 than ours. However, the higher density obtained by S00 may be real because their survey field is the LBG overdensity region. A summary of the space densities of high-z Lyα emitters is given in Table 6.

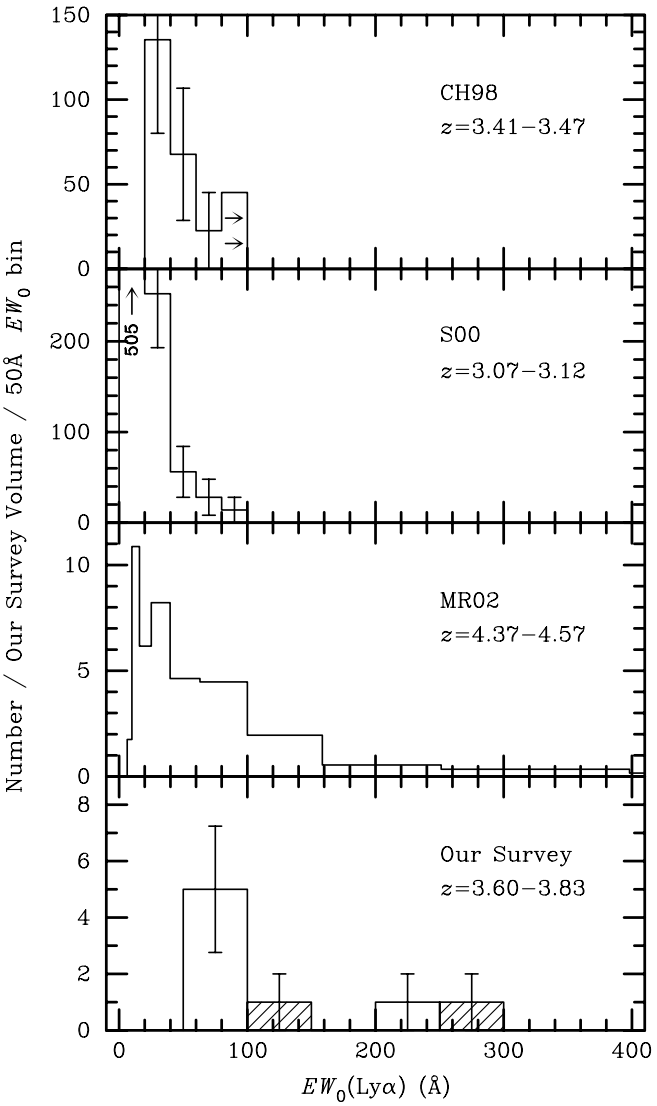

FIG. 21.—Comparison of frequency distributions of EW_0(Lyα) between our survey and those by CH98, S00, and MR01. The ordinate is the number of Lyα emitters per our survey volume per interval of $EW_0 = 50$ Å. The hatched region in our survey represents the marginal emitter candidates.

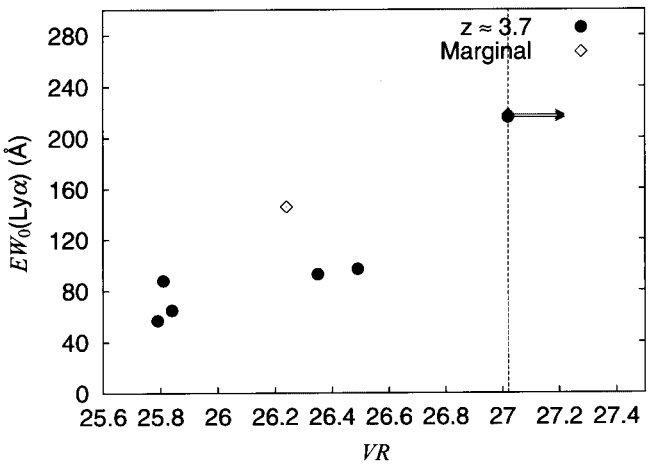

FIG. 22.—Diagram of EW_0(Lyα) versus *VR* magnitude for the six Lyα-emitter candidates at $z \approx 3.7$ (*filled circles*) and two marginal emitter candidates (*open diamonds*).

Then we investigate the Lyα luminosities of the $z \approx 3.7$ candidates. We assume that all the sources have a redshift of 3.717, which corresponds to the case that the Lyα emission is shifted to the central wavelength of IA574 filter. In Table 7 we give the Lyα luminosities for the six objects. The derived Lyα luminosities range from $\approx 5 \times 10^{42}$ to 1×10^{43} ergs s^{-1}, being slightly larger than those of CH98's sources. In Figure 23 we show the distribution of Lyα luminosities for our sample together with the results of CH98. Here we estimate the Lyα luminosities of CH98's sources using the cosmology adopted in this paper. It is shown that our survey probes higher luminosity sources with respect to the CH98 survey. It is likely that higher luminosity sources are fewer than lower luminosity ones. Therefore, in order to find such higher luminosity sources, it is necessary to perform wider-field surveys. Since our survey volume is wider by a factor of 10 than that of CH98, we can detect such higher luminosity Lyα emitters in our survey. On the other hand, our survey limit ($EW_{limit} = 250$ Å) is shallower by a factor of 2.5 than their limit ($EW_{limit} \approx 100$ Å). Therefore we miss a large number of lower luminosity Lyα emitters. Wide-field and very deep narrowband imaging surveys will be necessary to explore the nature of emission-line objects at high redshift (e.g., Taniguchi et al. 2001).

4.3. *Star Formation Density at $z \approx 3.7$*

Finally, we estimate the star formation rate for the six Lyα emitters at $z \approx 3.7$. Given the formula

$$\mathrm{SFR} = 7.9 \times 10^{-42} L(\mathrm{H}\alpha)\ M_\odot\ \mathrm{yr}^{-1}\ , \qquad (2)$$

where L(Hα) is the Hα luminosity in units of ergs per second (Kennicutt 1998), together with a relation,

$$L(\mathrm{Ly}\alpha) = 8.7 L(\mathrm{H}\alpha)\ , \qquad (3)$$

from case B recombination theory (Brocklehurst 1971), we can estimate the star formation rate using the Lyα luminosity:

$$\mathrm{SFR}(\mathrm{Ly}\alpha) = 9.1 \times 10^{-43} L(\mathrm{Ly}\alpha)\ M_\odot\ \mathrm{yr}^{-1} \qquad (4)$$

(see Hu et al. 2002). The results are given in the last column of Table 7. We note that the star formation rate derived here is reduced by the cosmic transmission (see the Appendix). The star formation rates range from 4.7 to 9.4 $M_\odot$ yr^{-1}, with an average of 6.4 ± 1.6 $M_\odot$ yr^{-1}. Although these values are typical of the Lyman break galaxies at $z \sim 3$–4 (e.g., Steidel et al. 1999 and references therein), the number density of the strong Lyα emitters like our sources is rather small (see Fig. 23).

We examine whether or not the SFR derived from the Lyα luminosity is consistent with that derived from the UV continuum luminosity for our sample. The observed i' magnitude can be converted to a UV continuum luminosity at $\lambda = 1600$ Å. Using the following relation (Kennicutt 1998; see also Madau et al. 1998),

$$\mathrm{SFR}(\mathrm{UV}) = 1.4 \times 10^{-28} L_\nu\ M_\odot\ \mathrm{yr}^{-1}\ , \qquad (5)$$

where L_ν is in units of ergs s^{-1} Hz^{-1}, we estimate the SFR based on the rest-frame UV (λ1600 Å) continuum luminosity for each object. The results are summarized in Table 8. Then, in Figure 24, we compare the two SFRs, SFR(Lyα)

TABLE 6
A SUMMARY OF THE LYα-EMITTER SURVEYS

Survey[a]	Field[b]	Field Type[c]	z_c[d]	(z_{min}, z_{max})[e]	V[f]	$EW_{lim}(Ly\alpha)$[g]	$N(Ly\alpha)$[h]	$n(Ly\alpha)$[i]
CH98	HDF	B	3.4	(3.41, 3.47)	5205	115	5	9.6×10^{-4}
CH98	SSA22	B	3.4	(3.41, 3.47)	5205	90	7	1.3×10^{-3}
K99.....	53W002	T	2.4	(2.32, 2.45)	85338	92	19	2.2×10^{-4}
K99.....	HU Aqr	B	2.4	(2.32, 2.45)	85338	241	1	1.2×10^{-5}
K99.....	NGC 6251	B	2.4	(2.32, 2.45)	85338	...	0	0
K99.....	53W002E	T	2.55	(2.49, 2.61)	78588	291	1	1.3×10^{-5}
K99.....	53W002N	T	2.55	(2.49, 2.61)	78588	155	1	1.3×10^{-5}
K99.....	53W002NE	T	2.55	(2.49, 2.61)	78588	184	4	5.1×10^{-5}
S00.....	LBGS[j]	B	3.09	(3.07, 3.12)	16741	80	72	4.3×10^{-3}
K00.....	Virgo[k]	B	3.14	(3.12, 3.15)	6020	...	8	1.3×10^{-3}
This study	Subaru/XMM	B	3.72	(3.60, 3.83)	93952	254	6	6.4×10^{-5}

[a] CH98 = Cowie & Hu 1998, K99 = Keel et al. 1999, S00 = Steidel et al. 2000, and K00 = Kudritzki et al. 2000.
[b] The name of the field.
[c] Field type: B = blank field, and T = targeted field.
[d] The central redshift corresponding to the central wavelength of the narrowband filter (λ_c).
[e] The minimum and maximum redshift covered by the narrowband filter.
[f] The comoving volume covered by the survey in units of $h_{0.7}^{-3}$ Mpc^3 with $\Omega_{matter} = 0.3$ and $\Omega_\Lambda = 0.7$.
[g] The smallest equivalent width of the Lyα emission detected in the survey in angstroms in the observed frame.
[h] The number of Lyα emitters found in the survey.
[i] The number density of Lyα emitters found in the survey in units of $h_{0.7}^3$ Mpc^{-3}.
[j] The LBG spike region.
[k] La Palma field (Mendez et al. 1997) in the Virgo Cluster.

and *SFR*(UV), for each object. It is shown that the two SFRs appear consistent within a factor of 2.

It is interesting to estimate the contribution of the star formation in the six Lyα-emitter candidates to the comoving cosmic star formation density (e.g., Madau et al. 1996). Integrating the star formation rates given in Table 7, we obtain the comoving star formation density for our sources, $\rho_{SFR} \sim 5.3 \times 10^{-4}\ M_\odot\ \mathrm{yr}^{-1}\ \mathrm{Mpc}^{-3}$. In this estimate we adopt an Einstein-de Sitter cosmology with $H_0 = 50\ \mathrm{km\ s}^{-1}\ \mathrm{Mpc}^{-1}$, following the manner of Madau et al. (1996).

In Figure 25 we compare this star formation rate density with those of previous studies compiled by Trentham, Blain, & Goldader (1999). We also show the results obtained by CH98 and K00. As shown in this figure, the star formation density derived in this study is much smaller than the previous estimates. However, note that no reddening correction is made for our data point (e.g., Pettini et al. 1998). It is also noted that we do not integrate the star formation density of Lyα emitters, assuming a certain luminosity function from a lower to a upper limit. The reason for this is that there is no reliable luminosity function for high-z Lyα emitters (see Fig. 23). Therefore future careful investigations will be absolutely necessary to estimate a more reliable contribution of Lyα emitters to the cosmic star formation density at high redshift.

TABLE 7
LYα LUMINOSITY AND STAR FORMATION RATE FOR THE LYα-EMITTER CANDIDATES AT $z \approx 3.7$

No.	EW_0 (Å)	$L(Ly\alpha)$ ($h_{0.7}^{-2}$ ergs s^{-1})	$SFR(Ly\alpha)$ ($h_{0.7}^{-2}\ M_\odot\ \mathrm{yr}^{-1}$)
1.....	216	1.04×10^{43}	9.4
2.....	97	5.20×10^{42}	4.7
3.....	93	6.14×10^{42}	5.6
4.....	88	8.27×10^{42}	7.5
5.....	65	6.02×10^{42}	5.5
6.....	57	6.48×10^{42}	5.9

5. SUMMARY

We have presented our optical intermediate-band ($\lambda_c = 5736$ Å and $\Delta\lambda = 280$ Å) and multicolor observations of the Subaru/XMM-Newton Deep Field obtained with Suprime-Cam on the 8.2 m Subaru telescope. All the data were obtained during the guaranteed time observations of the Suprime-Cam instrument. The intermediate-band image covered a sky area of $10\farcm62 \times 12\farcm40 \approx 132$ arcmin^2 in the Subaru/XMM-Newton Deep Field (Ouchi et al. 2001). Our survey volume amounts to 93,952 $h_{0.7}^{-3}$ Mpc^3 when we adopt a flat universe with $\Omega_{matter} = 0.3$, $\Omega_\Lambda = 0.7$, and $h = 0.7$, where $h = H_0/(100\ \mathrm{km\ s}^{-1}\ \mathrm{Mpc}^{-1})$. We give a summary of our results below.

1. In our survey we found 23 emission-line sources whose observed emission-line equivalent widths are greater than 250 Å. Their optical multicolor properties indicate six Lyα emission-line sources and two marginal candidate sources at $z \approx 3.7$ ($\Delta z \approx 0.22$) They are either intense starburst galaxies or active galactic nuclei–like quasars at $z \approx 3.7$. Among the remaining 15 emission-line objects, eight objects may be either [O II] λ3727 emitters at $z \approx 0.54$, Hβ emitters at $z \approx 0.18$, or [O III] λ5007 emitters at $z \approx 0.15$. The remaining seven objects have been found only in the IA574 image.

2. For the six Lyα emitters at $z \approx 3.7$ we obtain the average emission-line equivalent width of $\langle EW_0(Ly\alpha)\rangle \simeq 103 \pm 53$ Å. Their star formation rates range from 4.7 to 9.4 $M_\odot\ \mathrm{yr}^{-1}$ with an average of $6.4 \pm 1.6\ M_\odot\ \mathrm{yr}^{-1}$. Although these values are typical of those of the Lyman break galaxies at $z \sim 3$–4, the number density of the strong Lyα emitters like our sources appears rather small since the present survey is not deep enough to detect faint emission-line galaxies.

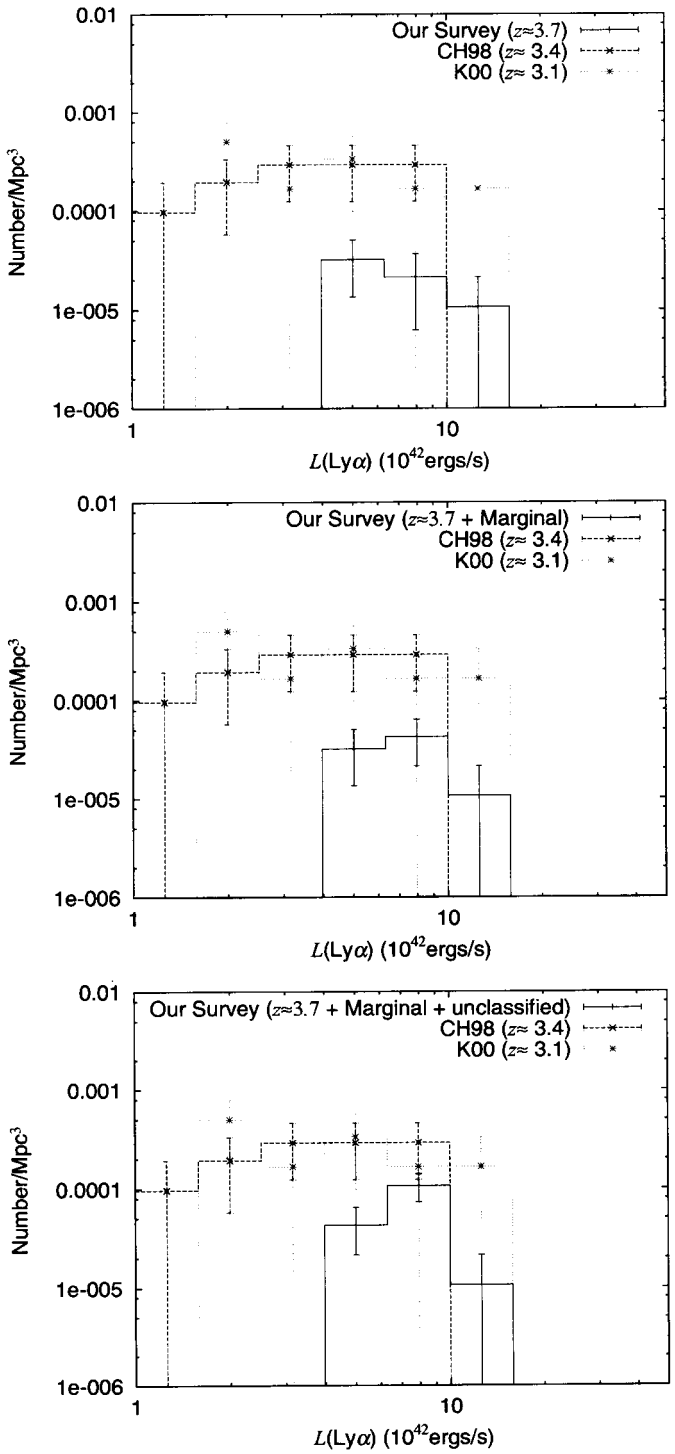

FIG. 23.—Distribution of Lyα luminosity compared with those derived by CH98 and K00.

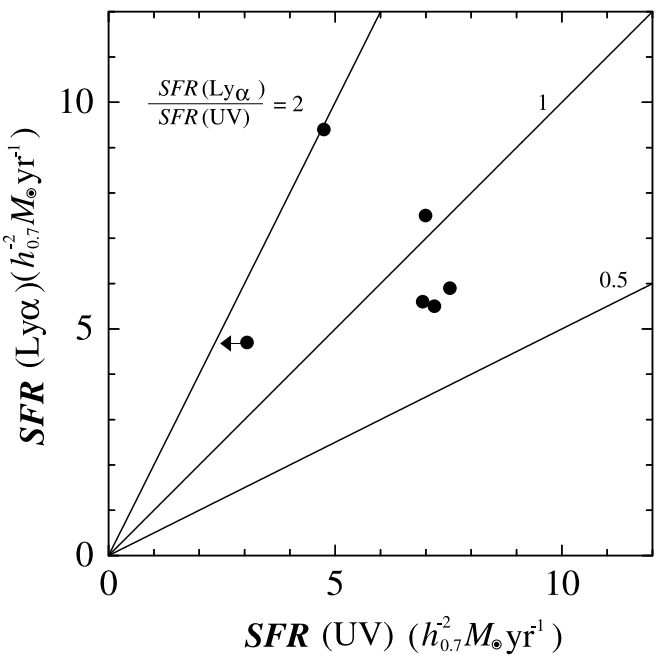

FIG. 24.—Comparison between *SFR*(Lyα) and *SFR*(UV) for the six Lyα emitters at $z \approx 3.7$.

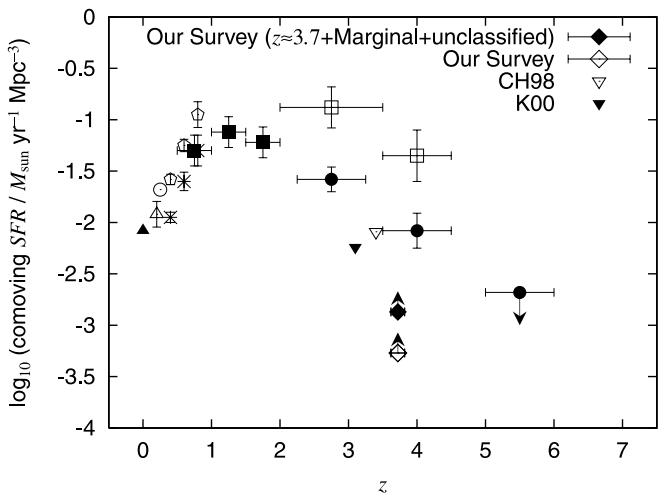

FIG. 25.—Star formation rate density at $z \approx 3.7$ derived in this study (*diamonds*) shown together with the previous investigations compiled by Trentham et al. (1999). The data sources are Gallego et al. (1996, *filled triangles*), Treyer et al. (1998, *open triangles*), Tresse & Maddox (1998, *open circles*), Lilly et al. (1996, *stars*), Hammer & Flores (1999, *open pentagons*), Connolly et al. (1997, *filled squares*), Madau et al. (1996, *filled circles*), and Pettini et al. (1998, *open squares*).

3. We estimated the contribution of star formation in the six Lyα-emitter candidates to the comoving cosmic star formation density (e.g., Madau et al. 1996). Integrating the star formation rates given in Table 6, we obtain the comoving star formation density for our sources, $\rho_{\rm SFR} \sim 5.4 \times 10^{-4}$ $M_\odot$ yr^{-1} Mpc^{-3}. In this estimate we adopt an Einstein-de Sitter cosmology with $H_0 = 50$ km s^{-1} Mpc^{-1}, following the manner of Madau et al. (1996).

We would like to thank the Subaru Telescope staff for their invaluable help in commissioning the Suprime-Cam, which made these difficult observations possible. Y. S., M. O., H. F., and F. N. acknowledge support from the Japan Society for the Promotion of Science (JSPS) through JSPS Research Fellowships for Young Scientists. This work was financially supported in part by the Ministry of Education, Science, Culture, and Technology (Nos. 10044052 and 10304013).

TABLE 8
UV Continuum Luminosity and Star Formation Rate for the Lyα-Emitter Candidates at $z \approx 3.7$

No.	i' (AB mag)	$f_\nu(i')$ (10^{-29} ergs s^{-1} cm^{-2} Hz^{-1})	L_{1600}[a] (10^{29} ergs s^{-1} Hz^{-1})	SFR(UV) ($h_{0.7}^{-2}$ $M_\odot$ yr^{-1})
1.....	26.16	0.125	0.339	4.75
2.....	>26.20	<0.120	<0.327	<4.58
3.....	25.75	0.182	0.495	6.93
4.....	25.74	0.184	0.500	6.99
5.....	25.71	0.189	0.514	7.19
6.....	25.66	0.198	0.538	7.53

[a] The UV continuum luminosity at $\lambda\lambda = 1600$ Å.

APPENDIX

THE EFFECT OF COSMIC TRANSMISSION ON THE EVALUATION OF LYα EMISSION

We demonstrate here how the value of min (VR−IA574, R−IA574) is affected by the absorption of neutral hydrogen gas clouds between the object and us, so-called the cosmic transmission. We also show how the cosmic transmission affects the detectability of Lyα-emitter candidates. In the text (§ 4.2) we evaluate the value of EW_{obs} simply from min (VR−IA574, R−IA574) and the value of EW_0 by dividing EW_{obs} by $(1 + z_{em})$, where z_{em} is the redshift of a Lyα-emitter candidate. Because of the cosmic transmission, the emission with wavelength of $\lambda < (1 + z_{em})$ $\lambda_{Ly\ \alpha}$ is dimmed as $F_{obs} = F_{int}\exp(-\tau_{eff})$, where F_{obs} is the observed flux, F_{int} is the intrinsic flux, $\exp(-\tau_{eff})$ is the cosmic transmission, and τ_{eff} is the effective optical depth. We have simulated the effect of cosmic transmission on min (VR−IA574, R−IA574) and EW_0 in the following way. For this simulation we prepare the SED with Lyα emission by adding the emission-line flux corresponding to EW_0^{model} with the Gaussian profile to the synthesized SED of young starburst galaxies, which is derived for the constant star formation rate with an age of 10^8 yr. We adopt the effective optical depth (τ_{eff}) formulated by Madau et al. (1996). Results are shown in Fig. 24. If the cosmic transmission is 1 ($\tau_{eff} = 0$), the min (VR−IA574, R−IA574) of Lyα emitters with $E_0^{obs} = 100$ Å is nearly constant and larger than 0.7 for redshifts between 3.61 and 3.82 (*long dashed line*, Fig. 24). On the other hand, adopting the average cosmic transmission, the value of min (VR−IA574, R−IA574) of Lyα emitters with $E_0^{obs} = 100$ Å (*solid line*) decreases with redshift and becomes smaller than 0.7 for redshifts higher than 3.65. The min (VR−IA574, R−IA574) of Lyα emitters with $E_0^{model} = 200$ Å is always larger than 0.7 for redshifts between 3.61 and 3.82, even if the effect of the cosmic transmission is taken into account (*dotted line*). These results imply that, because of the cosmic transmission, the detectability of Lyα emitters depends on the redshift of the galaxy, especially for Lyα emitters with smaller EW_0(Lyα). We also show the EW_0^{obs} calculated simply from the value of min (VR−IA574, R−IA574) in the bottom panel of Fig. 26. Because of the cosmic transmission, the value of EW_0^{obs} is smaller than EW_0^{model}. Taking account of this result, the star formation rate estimated in the text (§ 4.3) may be considered as a lower limit of the star formation rate.

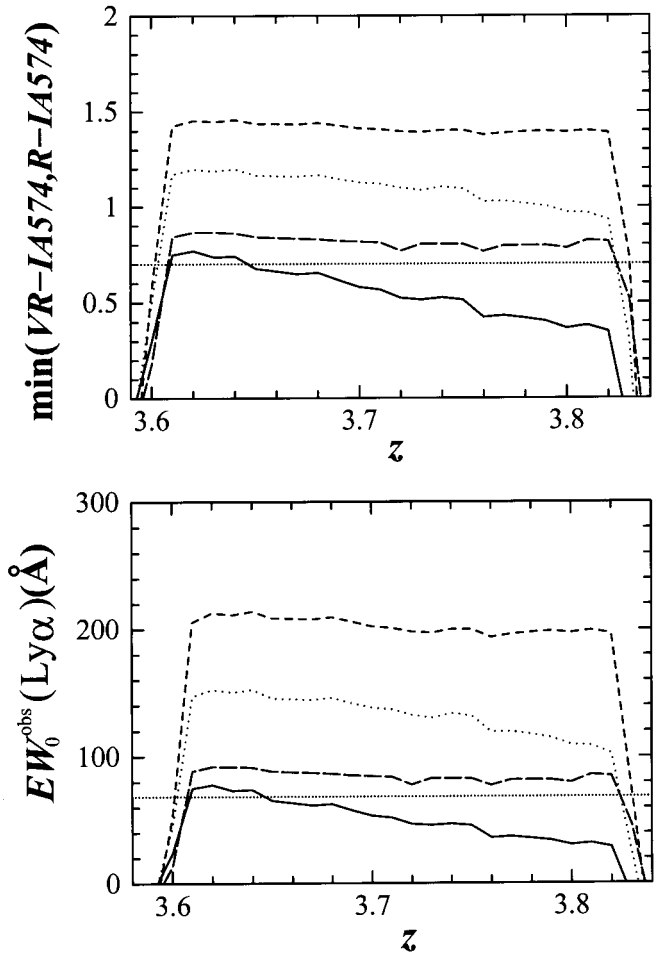

Fig. 26.—Predicted value of min (VR−IA574, R−IA574) (*top*) and E_0^{obs}(Lyα), which is simply evaluated from min (VR−IA574, R−IA574) as a function of z and EW_0^{model}(Lyα). The solid (*dotted*, *short-dashed*) line shows a model galaxy with EW_0^{model}(Lyα) = 100 (200, 400) Å affected by the cosmic transmission. We also show a model galaxy with EW_0^{model}(Lyα) = 100 Å and effective opacity of zero as a long dashed line.

REFERENCES

Baker, J. C., Hunstead, R. W., Bremer, M. N., Bland-Hawthorn, J., Athreya, R. M., & Barr, J. 2001, AJ, 121, 1821
Baldwin, J. A. 1977, ApJ, 214, 679
Bertin, E., & Arnouts, S. 1996, A&AS, 117, 393
Bland-Hawthorn, J., & Jones, H. 1997, preprint (astro-ph/9707315)
Bland-Hawthorn, J., van Bruegel, W., Gillingham, P. R., Baldry, I. K., & Jones, D. H. 2001, ApJ, 563, 611
Brocklehurst, M. 1971, MNRAS, 153, 471
Bruzual, A. G., & Charlot, S. 1993, ApJ, 405, 538
Coleman, G. D., Wu, C.-C., & Weedman, D. W. 1980, ApJS, 43, 393
Connolly, A. J., Szalay, A. S., Dickinson, M., Subbarao, M. U., & Brunner, R. J. 1997, ApJ, 486, L11
Cowie, L. L., & Hu, E. M. 1998, AJ, 115, 1319 (CH98)
Cowie, L. L., Songaila, A., Hu, E. M., & Cohen, J. G. 1996, AJ, 112, 839
Fukugita, M., Shimasaku, K., & Ichikawa, T. 1995, PASP, 107, 945
Gallego, J., Zamorano, J., Aragón-Salamanca, A., & Rego, M. 1996, ApJ, 459, L43
Hammer, F., & Flores, H. 1999, Dwarf Galaxies and Cosmology, ed. T. X. Thuan (Gif-sur-Yvette: Ed. Frontières), preprint (astro-ph/9806184)
Hayashino, T., et al. 2000, SPIE, 4008, 397
Hu, E. M., Cowie, L. L., & McMahon, R. G. 1998, ApJ, 502, L99
Hu, E. M., Cowie, L. L., McMahon, R. J., Capak, P., Iwamuro, F., Kneib, J.-P., Maihara, T., & Motohara, K. 2002, ApJ, 568, L75
Hu, E. M., & McMahon, R. G. 1996, Nature, 382, 231
Hu, E. M., McMahon, R. G., & Cowie, L. L. 1999, ApJ, 522, L9
Hu, E. M., McMahon, R. G., & Egami, E. 1996, ApJ, 459, L53
Jansen, R. A., Fabricant, D., Franx, M., & Caldwell, N. 2000, ApJS, 126, 331
Kaifu, N. 1998, Proc. SPIE, 3352, 14
Kajisawa, M., et al. 2000, PASJ, 52, 53
Keel, W. C., Cohen, S. H., Windhorst, R. A., & Waddington, I. 1999, AJ, 118, 2547
Kennicutt, R. C., Jr. 1998, ARA&A, 36, 189
Kinney, A. L., Bohlin, R. C., Calzetti, D., Panagia, N., & Wyse, R. F. G. 1993, ApJS, 86, 5
Kudritzki, R.-P., et al. 2000, ApJ, 536, 19 (K00)
Landolt, A. U. 1992, AJ, 104, 340
Lanzetta, K. M., Yahil, A., & Fernandez-Soto, A. 1996, Nature, 381, 759
Larson, R. B. 1974, MNRAS, 169, 229
Leitherer, C., & Heckman, T. M. 1995, ApJS, 96, 9
Lilly, S. J., Le Fevre, O., Hammer, F., & Crampton, D. 1996, ApJ, 460, L1
Loeb, A., & Barkana, R. 2001, ARA&A, 39, 19
Madau, P. 1995, ApJ, 441, 18
Madau, P., Ferguson, H. C., Dickinson, M. E., Giavalisco, M., Steidel, C. C., & Fruchter, A. 1996, MNRAS, 283, 1388
Madau, P., Pozzetti, L., & Dickinson, M. 1998, ApJ, 498, 106
Malhotra, S., & Rhoads, J. E. 2002, ApJ, 565, L71 (MR02)
Massey, P., Strobel, K., Barnes, J. V., & Anderson, E. 1988, ApJ, 328, 315
Meier, D. L. 1976, ApJ, 207, 343
Mendez, R. H., Guerrero, M. A., Freeman, K. C., Arnaboldi, M., Kudritzki, R. P., Hopp, U., Capaccioli, M., & Ford, H. 1997, ApJ, 491, L23
Miyazaki, S., Sekiguchi, M., Imi, K., Okada, N., Nakata, F. & Komiyama, Y. 1998, Proc. SPIE, 3355, 363
Ohyama, Y., Taniguchi, Y., Hibbard, J. E., & Vacca, W. D. 1999, AJ, 117, 2617
Oke, J. B. 1990, AJ, 99, 1621
Ouchi, M. 2001, Master's thesis, Univ. Tokyo
Ouchi, M., et al. 2001, ApJ, 558, L83
———. 2003, ApJ, in press
Pahre, M. A., & Djorgovski, S. D. 1995, ApJ, 449, L1
Partridge, R. B., & Peebles, P. J. E. 1967, ApJ, 147, 868
Pascarelle, S. M., Windhorst, R. A., Keel, W. C., & Odewahn, S. C. 1996, Nature, 383, 45
Petitjean, P., Pécontal, E., Valls-Gabaud, D., & Charlot, S. 1996, Nature, 380, 411
Pettini, M., et al. 1998, in Cosmic Origins: Evolution of Galaxies, Stars, Planets, and Life, ed. J. M. Shull, C. E. Woodward, & H. A. Thronson (San Francisco: ASP), 67
Pritchet, C. J. 1994, PASP, 106, 1052
Rhoads, J. E., & Malhotra, S. 2001, ApJ, 563, L5
Rhoads, J. E., Malhotra, S., Dey, A., Stern, D., Spinrad, H., & Januzzi, B. T. 2000, ApJ, 545, L85
Shioya, Y., et al. 2002, in preparation
Steidel, C. C., Adelberger, K. L., Giavalisco, M., Dickinson, M., & Pettini, M. 1999, ApJ, 519, 1
Steidel, C. C., Adelberger, K. L., Shapley, A. E., Pettini, M., Dickinson, M., & Giavalisco, M. 2000, ApJ, 532, 170 (S00)
Steidel, C. C., Giavalisco, M., Dickinson, M., & Adelberger, K. L. 1996a, AJ, 112, 352
Steidel, C. C., Giavalisco, M., Pettini, M., Dickinson, M., & Adelberger, K. L. 1996b, ApJ, 462, L17
Stern, D., Bunker, A., Spinrad, H., & Dey, A. 2000, ApJ, 537, 73
Stockton, A., & Ridgway, S. E. 1998, AJ, 115, 1340
Taniguchi, Y. 2001, The Japan-Germany Workshop on Studies of Galaxies in the Young Universe with New Generation Telescopes, ed. N. Arimoto & W. Duschul, in press
Taniguchi, Y., & Shioya, Y. 2000, ApJ, 532, L13
Taniguchi, Y., Shioya, Y., & Kakazu, Y. 2001, ApJ, 562, L15
Thompson, D., Mannucci, F., & Beckwith, S. V. W. 1996, AJ, 112, 1794
Trentham, N., Blain, A. W., Goldader, J. 1999, MNRAS, 305, 61
Tresse, L., & Maddox, S. J. 1998, ApJ, 495, 691
Treyer, M. A., Ellis, R. S., Milliard, B., Donas, J., & Bridges, T. J. 1998, MNRAS, 300, 303
Vanden Berk, D. E., et al. 2001, AJ, 122, 549
Yagi, M., Kashikawa, N., Sekiguchi, M., Doi, M., Yasuda, N., Shimasaku, K., & Okamura, S. 2002, AJ, 123, 66
Yahata, N., Lanzetta, K. M., Chen, H.-W., Fernandez-Soto, A., Pascarelle, S. M., Yahil, A., & Puetter, R. C. 2000, ApJ, 538, 493
Yoshida, T., et al. 2002, in preparation